PREDICTION OF DIFFRACTION FORCES ON A WAVE ENERGY CONVERTER USING BEM AND CFD APPROACH

by

Akshith Subramanian

A thesis submitted to the faculty of
The University of North Carolina at Charlotte
in partial fulfillment of the requirements
for the degree of Master of Science in
Mechanical Engineering

Charlotte

2018

Approved by:

Dr. Navid Goudarzi

Dr. Russell Keanini

Dr. Mesbah Uddin

ABSTRACT

AKSHITH SUBRAMANIAN. Prediction of Diffraction Forces on a Wave Energy Converter using BEM and CFD approach. (Under the direction of DR. NAVID GOUDARZI)

Alternative energy sources address concerns about fossil fuels such as environmental degradation, public health, and finite energy source. Compared to wind and solar powers, wave power has a higher energy density and is easier to forecast. However, non-linear, complex, and turbulent nature of oceans necessitate a more in-depth flow field analysis before the deployment of wave energy converters (WECs). This research explores the performance of a two-point body absorber WEC, Reference Model 3 (RM3) introduced by the Department of Energy (DOE), to be deployed in North Carolina shores. The wave data from US 192 and US 430 buoy stations were used to calculate the hydrodynamic forces, with focus on the diffraction and Froude-Krylov forces in this work, on the RM3 using

1. DOE WEC-Sim, a boundary element method-based (BEM) approach
2. Computational fluid dynamics (CFD), a finite volume method-based approach

In the first approach, a full-scale model of RM3 was studied. In the second approach, using the wave characteristics and ocean depth along the North Carolina shores, three scalded RM3 models: 50^{th}, 100^{th}, and 200^{th}, were studied. The developed CFD model based on the volume of fluid (VoF) Eulerian multiphase flow was initially validated with published computational and experimental literature. The realizable $k-\epsilon$ turbulence model was employed to study the effects of ocean wave turbulence. The validated model was used to study the generated 5^{th} order approximation Stokes wave on the RM3. The grid analysis, using cell sizes ranging from 2.8 million to 9.4 million, verified the appropriate mesh resolution of 7.2 million on the floating part of the RM3. The main challenges faced during the computational domain setup such as free-surface mesh refinement, boundary conditions, preventing wave reflection,

and scaling the model are elaborated and appropriate solutions are stated. Next step of this research includes modeling the radiation forces to determine the total hydrodynamic forces on the RM3 when deployed as a stand-alone or an array along the North Carolina shores. Also, ongoing experimental testing within the NADGOD research group on scaled RM3 models will validated and verify the developed CFD model.

ACKNOWLEDGEMENTS

I would first like to thank my thesis advisor Dr. Navid Goudarzi at University of North Carolina at Charlotte. The door to Prof. Goudarzi's office was always open whenever I ran into a difficulty or had a question, during the course of my research. He consistently steered me in the right the direction whenever he thought I needed it. I would also like to thank my parents and my brother for their love and support, my friends Satyam Shukla, Shreyas Vaidyanath, Pauras Sawant, Rashmi Nair and many others for lifting me up when I felt low.

TABLE OF CONTENTS

LIST OF FIGURES vii

LIST OF TABLES viii

CHAPTER 1: INTRODUCTION 1

CHAPTER 2: HYDRODYNAMICS 7

2.1. WEC-Sim 9

CHAPTER 3: METHODOLOGY 11

3.1. WEC-Sim Approach 12

3.2. CFD Based Approach 14

3.2.1. Challenges 19

CHAPTER 4: RESULTS 21

4.1. WEC-Sim 21

4.2. Validation Case 24

4.3. Reference Model 3 27

4.4. Conclusion 34

4.5. Future Scope 35

REFERENCES 36

APPENDIX A: StarCCM+ 40

LIST OF FIGURES

FIGURE 1.1: Global temperature change over the 20^{th} century [1] 1

FIGURE 1.2: Power conversion chains (PCC) from mechanical to electrical energy [2] 5

FIGURE 3.1: Reference Model 3 11

FIGURE 3.2: WEC-Sim methodology [3] 12

FIGURE 3.3: Numerical wave tank (NWT) 16

FIGURE 4.1: Pitch force on float [4] 22

FIGURE 4.2: Surge force on spar [4] 23

FIGURE 4.3: Volume mesh result on the studied computational domain 24

FIGURE 4.4: Mesh refinement at air-water interface 25

FIGURE 4.5: Mesh sensitivity analysis 25

FIGURE 4.6: Heave force 26

FIGURE 4.7: Wall y+ value for the sphere 26

FIGURE 4.8: The mesh refinement along the free surface 27

FIGURE 4.9: Pitch force on 50^{th} scaled RM3 28

FIGURE 4.10: Pitch force on 100^{th} scaled RM3 29

FIGURE 4.11: Pitch force on 200^{th} scaled RM3 30

FIGURE 4.12: Heave force on 50^{th} scaled RM3 31

FIGURE 4.13: Heave force on 100^{th} scaled RM3 32

FIGURE 4.14: Heave force on 200^{th} scaled RM3 33

FIGURE 4.15: Wall Y+ over 50^{th} scaled RM3 model 34

LIST OF TABLES

TABLE 1.1: DOE definded Reference Models [5]. 3

TABLE 1.2: Deployed WEC devices [6] 4

TABLE 3.1: Physics models implemented 18

TABLE 4.1: Scaled RM3 Dimensions 27

LIST OF ABBREVIATIONS

BEM Boundary Element Method

CFD Computational Fluid Dynamics

Fr Froude Number

MHK Marine and Hydrokinetic

NDBC National Data Buoy Center

NREL National Renewable Energy Laboratory

NSE Navier-Stokes Equation

NWT Numerical Wave Tank

PCC Power Conversion Chain

PTO Power Take-Off

Re Reynolds Number

RM3 Reference Model 3

RMP Reference Model Project

SNL Sandia National Laboratory

VoF Volume of Fluid

Wb Weber Number

WEC Wave Energy Converter

CHAPTER 1: INTRODUCTION

To reduce the growing concerns on the global warming due to human activity or tropical deforestation, there is a significant need to reduce the heat-trapping emissions. Over 80 percent of the global energy requirement comes from fossil fuels [7]. Although there has been a significant increase in efficiency of energy being extracted from fossil fuels, the rate of increase in global warming is rapidly reaching irreparable stages. If steps and measures are not taken immediately to shift the dependency from non-renewable to renewable sources of energy, the climate change taking place might be irreversible. The Remote Sensing Systems (RSS) satellite actively used to measure global temperatures, has measured an increase of 2° Celsius in the 20th Century [1].

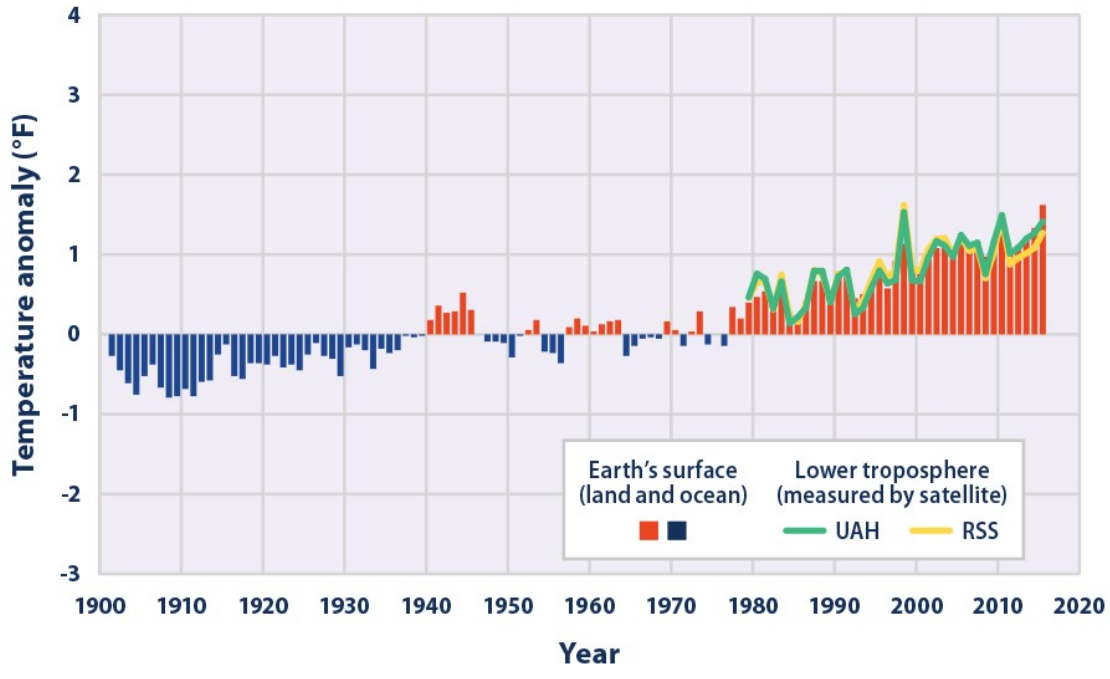

Figure 1.1: Global temperature change over the 20^{th} century [1]

These statistical data played a critical role in accelerating the change from non-renewable sources of energy to renewables. The total world renewable energy capacity had a 9% increase in 2017 as compared to that in 2015. Many countries have started changing their energy policies and are striving to ensure a shift towards renewable energy sources [8]. More than half of the population of the US is currently living near coastlines [9]. Marine and hydrokinetic (MHK) energy resources would be a suitable form of renewable energy resource for power production in these regions. In 2016, 78% of the US energy needs were met from non-renewable sources of energy such as natural gas, petroleum and coal. Renewables contributed to just 12% of the total energy dependence and 6.5% of this was attributed to hydro-power [10]. Since hydro-power also comprises of dams built to harvest energy, there is a tremendous scope for improvement in wave and tidal energy harvesting techniques.

Wave energy converter (WEC) devices are gaining rapid popularity amongst the renewable energy sector due to the advantages of predictability and stability of wave energy when compared to other forms of renewables. Wave energy is a vastly untapped source of energy for power generation. It is estimated that the theoretical and technical wave energy resource potentials are nearly 1594-2460 TWh/yr and 898-1229 TWh/yr, respectively [11]. Hence, there have been increased efforts to promote the development of innovative designs for wave energy converters. For this purpose, the DOE in collaboration with Sandia National Laboratory (SNL) and National Renewable Energy Laboratory (NREL), developed an open-source code WEC-Sim based on MATLAB which allows users to validate new designs for WEC devices. In addition to this, they also defined a Reference Model Project (RMP), which aimed at setting up RM performance specifications benchmarks based on studied sites, as shown in Table 1.1:

Table 1.1: DOE definded Reference Models [5].

Reference Model Number	Type
1	Tidal current turbine
2	River current turbine
3	Wave point absorber
4	Ocean current turbine
5	Oscillating surge - wave energy converter
6	Floating oscillating surge - wave energy converter

The RM1 is a variable-speed variable-pitch (VSVP) axial flow tidal turbine device, developed for Tacoma Narrow tidal current. There are several other types of WEC devices tested at different locations over the years. A few examples of those can be seen in Table 1.2.

The RM3 was used in this research. RM3 is a two-body point absorber device with a float oscillating on a vertical spar (column), while the whole device is moored to the seabed to prevent roll and yaw movement of the device [12]. As the body interacts with waves, the float moves vertically on the spar.

These devices based on their deployment site, implement different power conversion chains (PCC). PCC's convert the mechanical energy from ocean waves into clean usable electrical energy. Most WEC's convert a linear motion, rotatory motion, or fluid capture method to generate electric power.

Figure 1.2 illustrates different PCCs. The left side of the figure shows an intellectualized energy conversion flow. The black arrows show the possible energy flow paths and the color legends have been used to determine the technological readiness levels as of 2016 [2]. The Direct drive method makes use of the principles of electro-

Table 1.2: Deployed WEC devices [6]

Name	Structure	Classification	Energy mode	PTO	Rated power (kW)	Reference
AquaBuoy	Two-body floating system	Point absorber	Heave	High-head water turbine	250	[13]
AWS	Two-body submerged system	Point absorber	Heave	Linear generator	2470	[14]
Langlee	Semi-submerged three-body structure	Oscillating wave surge converter	Surge	Hydraulic motor	1665	[15]
OEbuoy	Single-body floating system	Oscillating water column	Surge	Bidirectional air turbine	2880	[6]
Pelamis	Four-body floating system	Attenuator	Heave and Sway	Hydraulic motor	750	[16]
Pontoon	Multi-body floating structure	Multiple point absorber	Heave	High-head water turbine	3619	[6]
SeaPower	Two-body platform	Attenuator	Pitch	Pump or hydraulic motor	3587	[6]

magnetic induction to convert the mechanical energy from the wave motion to clean electrical energy; the surface float of the device comprises of a magnetic core and the spar (vertical column) has winding coils, the electrical output is produced due to the relative motion of the surface float with respect to the spar [5]. In an indirect drive PCC system, as the float moves to a lower position on the vertical column, water enters into the created low-pressure zone. This water is allowed to pass through to the bottom of the system where its potential energy is used to drive a turbine to produce the electrical energy [2]. The whole system is moored to the seabed to prevent movement and the surge of the device [17].

Experimental testing of WEC devices in wave tanks, trying to recreate environmental conditions followed by prototype testing in seas is inevitable, but with the increase in computational processing power over the years has made it possible to run CFD

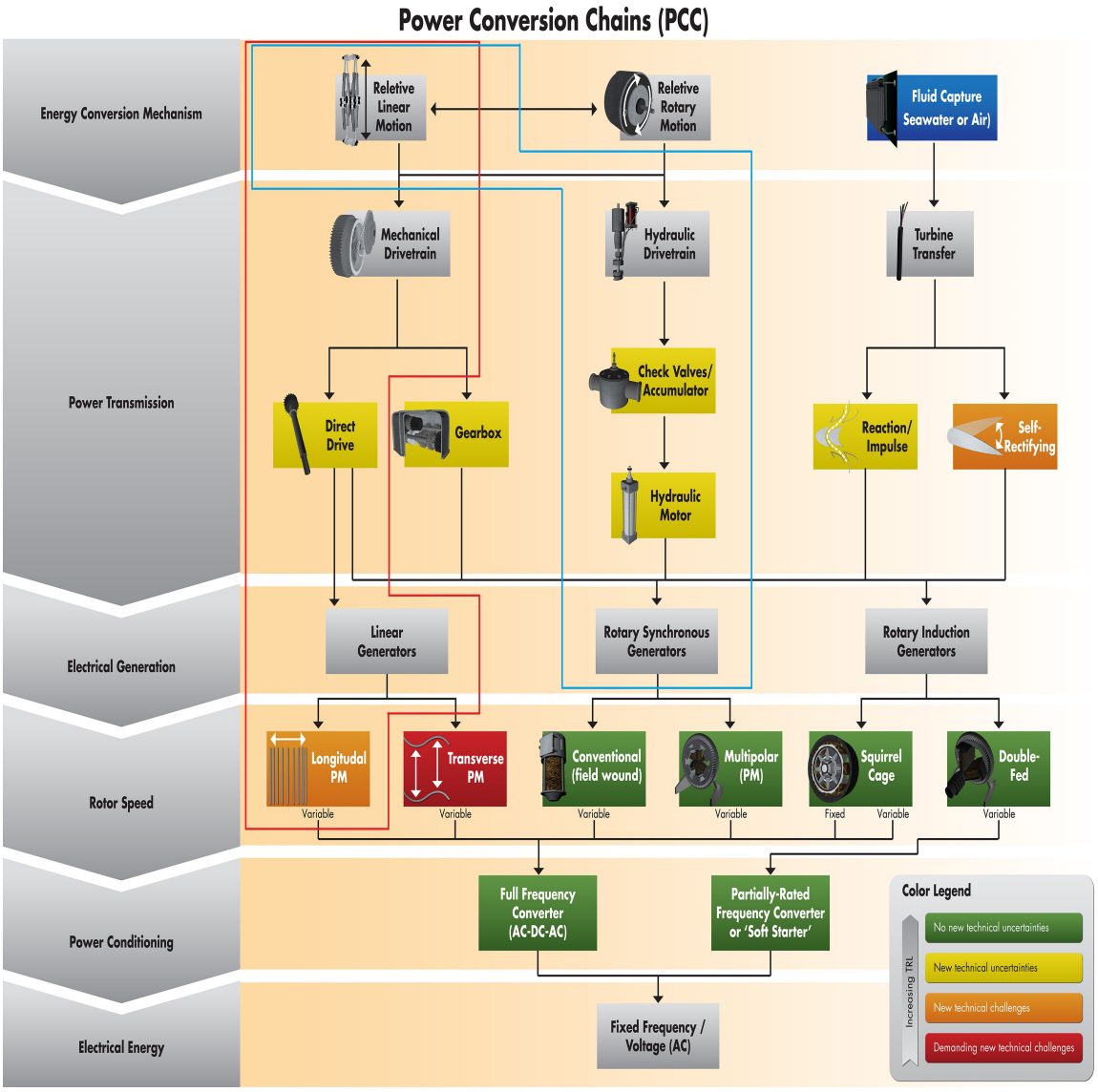

Figure 1.2: Power conversion chains (PCC) from mechanical to electrical energy [2]

simulations on these devices while simulating environmental conditions to give an initial validation for the design before proceeding to expensive and time consuming experimental testing. Numerical wave tanks (NWT) are developed using different techniques including boundary element method (BEM) and finite volume method (FVM). Numerical waves being generated are generated at the inlet boundary and damped near the outlet boundary [18]. Wu and Hu (2004) [19] made use of a finite element method (FEM) NWT to simulate the nonlinear interaction between water

waves and a floating cylinder. Hadzic et al. (2005) [20] simulated a 2-D NWT to determine the motion of a floating rigid body with up to six degrees of freedom as it is subjected to large amplitude of waves. Agamloh et al. (2008) [21] made use of a commercial CFD package to develop a 3-D NWT, to model the fluid-structure interaction between water waves and a cylindrical ocean wave energy converter.

Performance testing of RM3 has been done only to validate the WEC-Sim code and no reliable source of data exists for performance validation of the RM3 for North Carolina shore. The aim of this thesis is to use StarCCM+, a commercial CFD package, to calculate the hydrodynamic forces on the RM3 using North Carolina wave data. This computational platform facilitates the testing of innovative designs for WEC's at a reduced cost and risk of experimental testing. Long-term Wave data were collected from two buoys (US430 and US192) of the North Carolina shore from National Data Buoy Center (NDBC). A MATLAB code was developed to filter the data and estimate the average output power density and wave characteristics [22].

CHAPTER 2: HYDRODYNAMICS

The hydrodynamic forces acting on a floating body can be classified into seven force components:

- wave diffraction forces.
- wave radiation forces.
- viscous damping forces.
- buoyancy restoring forces.
- mooring forces
- power take-off forces
- morrison element forces

The wave diffraction forces are the forces being experienced by the body as the incident wave is dispersed in the direction of wave motion and can be estimated by assuming potential flow theory which simplifies the numerical calculations. In accordance with potential flow theory, the potential of a floating body in wave motion is a superposition of the potential due to the radiation potentials due to the six body motions Φ_j, the undisturbed incoming wave Φ_w, and the potential due to diffraction of the undisturbed incoming wave Φ_d [23]. The wave radiation forces are due to the vertical oscillatory movement of the body in the wave motion. These forces include the viscous damping forces and the nonlinear Froude-Krylov forces. The nonlinear forces are calculated by integrating the static and dynamic pressures over each panel along wetted body surface at each time step. Since linear wave theory is applied to calculate the flow velocity and pressure field, there is a need for a correction. This

is done by applying Wheeler's stretching method, which corrects the instantaneous wave elevation (wave height) and makes it equal to the water depth while calculating the new flow velocity and pressure [24]. The mooring forces experienced by the body are due to the mooring lines which restrict the movement of the body in the sea. The mooring forces help to determine the stress on the mooring cables and assist in determining suitable materials for the mooring system [17]. The power take-off (PTO) forces are the forces experienced by the body while there is conversion of mechanical energy to electrical energy. The PTO forces are maximum when a hydraulic power conversion system is used due to the entry of water into the system [2]. The Morison Equation assumes that the fluid forces in an oscillating flow on a structure of small cylinders or other similar geometries arise partly from pressure effects from potential flow and partly from viscous effects. A small cylinder implies that the diameter, D, is small relative to the wave length, λ_w , which is generally met when D/λ_w<0.1-0.2. If this condition is not met, wave diffraction effects have to be accounted for. Provided the geometries are small, the resulting force can be approximated by a modified Morison formulation [25].

According to the potential flow theory, the total potential on a body can be defined as in equation 2.1:

$$\Phi = \sum_{j=1}^{6} \Phi_j + \Phi_w + \Phi_d \tag{2.1}$$

Applying the kinematic boundary conditions for free-surface of the water to the space-dependent part of the velocity potential results in:

$$\Phi_0 = \frac{\zeta_0 g}{\omega} . \frac{\cosh k(h_0 + z)}{\cosh kh} . e^{ik(x\cos(\mu) + y\sin(\mu))} \tag{2.2}$$

where Φ_0 is the velocity potential

ζ_0 is the amplitude of undisturbed wave (m)

$k = 2\pi/\lambda$ is the wave number (rad/m)

λ is the wavelength (m)

ω is the wave frequency (rad/s)

μ is the wave direction (rad); zero for wave travelling in positive x-direction

h_0 is the instantaneous water depth (m)

h is the water depth (m)

The diffraction forces are then calculated from the velocity potentials.

Radiation forces are the reaction forces of the body to the incident wave potential. The radiation potential tends to zero as the distance R of the radiated wave from the body increases [23].

$$\lim_{R\to\infty} \Phi_r = 0 \tag{2.3}$$

The radiation hydrodynamic forces can be written as

$$\vec{F_r} = \rho \iint_S (\frac{\partial}{\partial t} \sum_{j=1}^{6} \Phi_j v_j)\vec{n}.dS \tag{2.4}$$

And the Moments can be expressed as

$$\vec{M_r} = \rho \iint_S (\frac{\partial}{\partial t} \sum_{j=1}^{6} \Phi_j v_j)(\vec{r} \times \vec{n}).dS \tag{2.5}$$

where, ρ is the density of the fluid, v_j is the oscillatory velocity of the body, $\vec{n}$ is the outward normal vector on the surface dS and $\vec{r}$ is the position vector of surface dS with respect to the coordinate system. The components of force and moments are given by [23] $\vec{F_r} = (X_{r1}, X_{r2}, X_{r3})$ and $\vec{M_r} = (X_{r4}, X_{r5}, X_{r6})$ respectively.

where

$$X_{rk} = \frac{dv_j}{dt}\rho \iint_S \Phi_j \frac{\partial \Phi_k}{\partial n}.dS \tag{2.6}$$

for $k = 1, ...6$.

2.1 WEC-Sim

The analysis of wave diffraction and radiation by a body at or near free surface requires the solution of a boundary value problem based on Laplace's equation. Since

the problem involves an unbounded domain, the integral equation method gives certain advantages to the solution. For a boundary element method (BEM) approach, the submerged body is discretized by a set of quadrilateral or triangular flat panels [26]. To use BEM to solve boundary value problem, the problem needs to be transformed into an equivalent boundary integral equation problem. Green theorem is used to transform the fundamental solution to set of intergral equations which are solved using BEM [27]. Recent studies by Liu [28] [29], Eatock Taylor and Chau [30], and Eatock Taylor and Teng [31] have shown higher order element methods to provide more accurate results than a constant panel method. With the frequency domain problem of wave interaction with a device in the horizontal unbounded domain, integrations on the free surface, device, and seabed can be eliminated by the application of Green function satisfying the scattering wave boundary condition on those surfaces. Thus, with Green function being applied with the BEM approach, only the body surface needs to be discretized to distribute the unknowns on the body surface which helps to reduce the computational load [32]. DOE in collaboration with Sandia National Laboratory (SNL) and National Renewable Energy Laboratory (NREL), developed an open-source MATLAB code, called WEC-Sim that allows users to validate different designs for WEC devices. A frequency-domain boundary element method (BEM) solver uses linear coefficients to solve the system dynamics in the time domain. It divides the hydrodynamic forces into radiation and diffraction components and solves the Laplace equation (assuming the flow is inviscid, incompressible, and irrotational) for the velocity potential for each of them individually.

CHAPTER 3: METHODOLOGY

The diffraction forces are calculated for the RM3, a two-body floating point absorber, using the North Carolina wave data. Figure 3.1 illustrates the RM3 with its two main components: the surface float and spar, which has a reaction plate at the end. The float can have a 4 m displacement on the vertical column/spar. The RM3 is intended for deployment in 40 m to 100 m water depth and moored to the seabed. It uses a hydraulic power conversion system inside the spar with a rated power of 300 kW when the system is operating at resonance with the incoming wave [5].

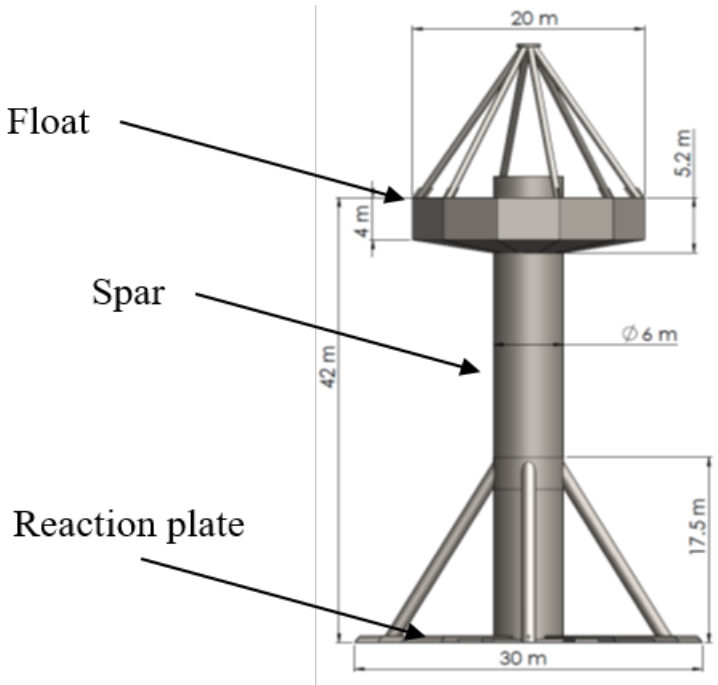

Figure 3.1: Reference Model 3

3.1 WEC-Sim Approach

Figure 3.2 illustrates the four major steps in implementing WEC-Sim:

1. Pre-processing
2. WEC-Sim inputs
3. Creating Simulink model
4. Running WEC-Sim

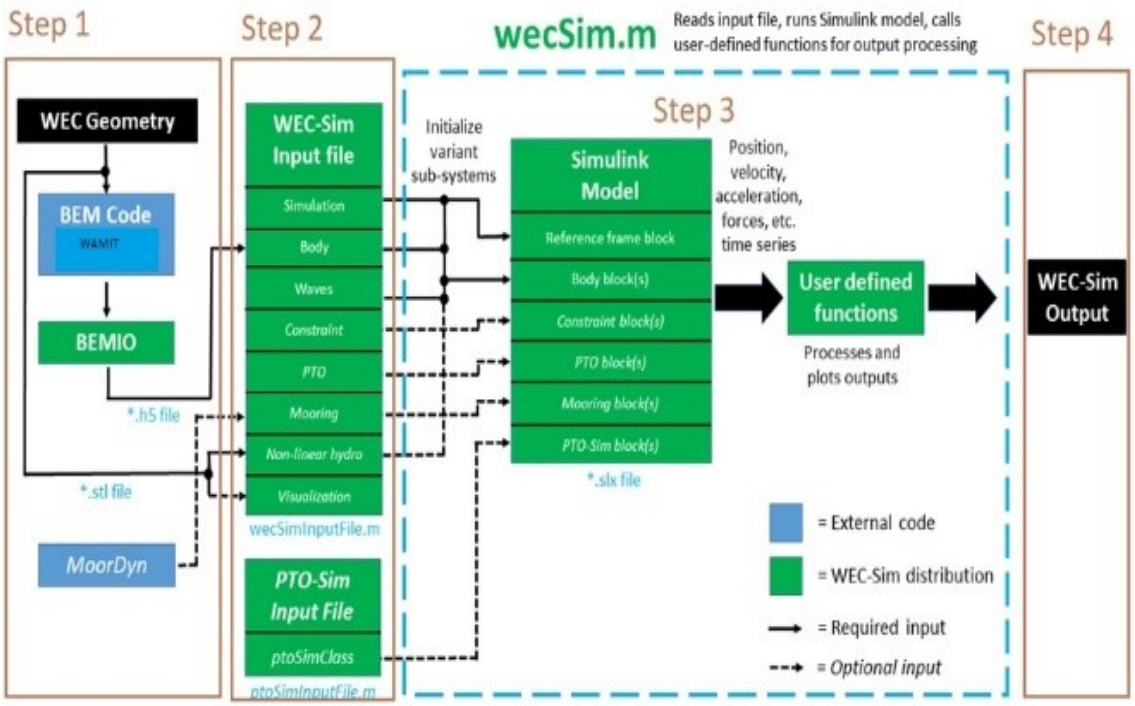

Figure 3.2: WEC-Sim methodology [3]

In pre-processing, a BEM-based code, WAMIT, is used to calculate the hydrodynamic force coefficients. WAMIT is one of the well-known codes for analyzing wave interactions with offshore platforms and floating bodies such as RM3. The body geometry is imported as a geometric data file (.GDF), along with a potential control file (.POT) and force control file (.FRC) are input to the BEM solver [33]. The body mass, water depth, wave heights, wave time-periods, and degrees of motion of the body are specified. The BEM solver then calculates the hydrodynamic force coeffi-

cients which are then inputs to the step 2, WEC-Sim inputs. In the WEC-Sim inputs step, the RM3 configuration specifications such as mass, moment of inertia, center of gravity, as well as the hydrodynamic force coefficients are inserted. Next, a Simulink model is created with the help of an inbuilt library of WEC components and the degrees of freedom of the device are set. The input parameters are set such that they overlay those specified in the input file. In step 4, WEC-Sim output, the desired plots are specified. The use of WEC-Sim is limited to visualization of the hydrodynamic forces on the body. There is very little that can be done in terms of post-processing of the data gathered from WEC-Sim. Hence, in this work, a CFD model was developed for determining the hydrodynamics forces on RM3.

3.2 CFD Based Approach

In this Section, the diffraction forces on RM3 due to incoming one-directional waves is studied numerically in StarCCM+, a commercial CFD software. The CFD simulation were conducted on 50^{th}, 100^{th}, and 200^{th} scaled-RM3 models. The governing equation for a CFD simulation is based on Navier-Stokes Equation (NSE) given by conservation of mass (continuity), given by equations 3.1, 3.2, 3.3 respectively.

$$\frac{\partial \rho}{\partial t} = \nabla.(\rho v) = 0 \tag{3.1}$$

conservation of momentum,

$$\frac{\partial \rho v}{\partial t} + \nabla.(\rho v * v) = \nabla.\sigma + f_b \tag{3.2}$$

and conservation of energy

$$\frac{\partial (\rho E)}{\partial t} + \nabla.(\rho E * v) = f_b + \nabla.(v.\sigma) + \nabla.q + S_E \tag{3.3}$$

The pressure fields are calculated from the pressure poisons equation (PPE) which is derived from the NSE given by equation when written in its primitive form as follows [34]. Equation 3.4 gives the momentum equation

$$u_t + (u.\nabla)u = \mu \Delta u - \nabla p + f \tag{3.4}$$

Equation 3.5 is the divergence free constraint which is derived from the conservation of mass, as under incompressible conditions the net flux through the boundary must be zero.

$$\nabla.u = 0 \tag{3.5}$$

where $u_t(x,t)$ is the velocity, μ is the kinematic viscosity of the fluid, $p(x,t)$ the pressure, $f(x,t)$ is the body force, ∇ is the gradient operator, and Δ is the Laplacian operator ($\Delta = \nabla^2$).

Divergence of equation 3.4 is taken and the divergence free condition from equation 3.5 is used, and it can be written as follows

$$\nabla.(u_t + (u.\Delta)u) = \nabla.(\mu.u - \nabla p + f) \tag{3.6}$$

The LHS can be written as follows

$$\nabla.(u_t + (u.\Delta)u) = \frac{\partial}{\partial t}(\nabla.u) + \nabla.(u.\nabla)u = \nabla.(u.\nabla)u \tag{3.7}$$

The RHS can be written as follows

$$\nabla.(\mu u - \nabla p + f) = \mu\Delta(\nabla.u) - \Delta p + \nabla.f = -\Delta p + \nabla.f \tag{3.8}$$

Rearranging equations 3.7 and 3.8 we get the pressure poisson equation (PPE).

$$\Delta p = \nabla.(f - u.\nabla)u) \tag{3.9}$$

Dimensional analysis was required to reduce the number of variables as well as interpreting data obtained from the CFD model to the full-scale prototype. For determining the hydrodynamic flow characteristics of the scaled model, the Froude (Fr), Reynolds (Re), and Weber (Wb) numbers given by equations 3.10 [35], 3.11 [36] and 3.12 [37], respectively, were studied. The Re number should be studied in almost all different flow regimes. The Fr and Wb numbers become important in free-surface flow analysis. Since the RM3 is assumed to be located in an intermediate water depth, the variation of Fr number becomes more important than the Wb number. In other words, the gravitational effects are considered to be more important than viscosity and surface tension of water [36].

$$Fr = \frac{U}{\sqrt{gL}} \tag{3.10}$$

$$Re = \frac{UL}{\nu} \tag{3.11}$$

$$Wb = \frac{\rho U^2 L}{\sigma} \tag{3.12}$$

where U is the free-stream velocity of the fluid, g is the gravitational acceleration, L is the characteristic/hydrodynamic length, ν is the kinematic viscosity of the fluid, and σ is the surface tension.

Figure 3.3 illustrates the numerical wave tank (NWT) or computational domain.

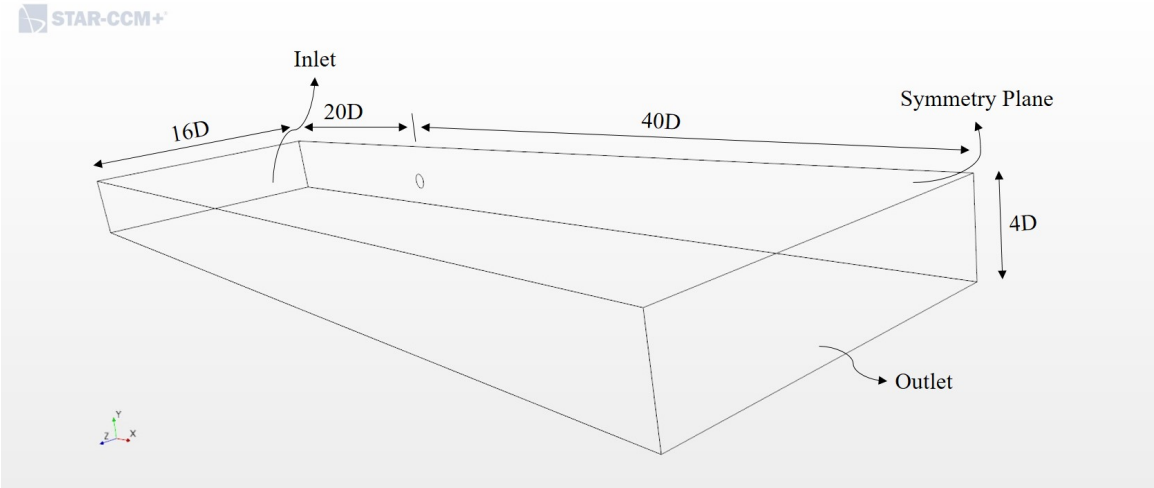

Figure 3.3: Numerical wave tank (NWT)

Using the RM3 location as the reference, the NWT is 20D to the front, 40D to the back, 16D wide and 4D in height. The water surface is at 60% of the computational domain height. A symmetry plane at the RM3 location was used to reduce the computational cost (mesh size and computational time). An Eulerian multiphase with a volume of fluid (VoF) method and a segregated flow solver was applied for this case. An implicit unsteady time discretization with time steps to be 200^{th} of the wave time-period was used. Realizable $k - \epsilon$ turbulence model was employed.

The non-linear hydrodynamic analysis method from the work of Adian et al. [38] was developed and validated first. Following the validation stage, the numerical model was modified to consider the RM3 model geometry and North Carolina wave characteristics in this research. To calculate the hydrodynamic diffraction forces on the body and neglect the effects of non-linearity due to the incident waves, the intermediate depth water conditions and a stokes 5^{th} order wave were used. The wave data for this work was derived from National Oceanic and Atmospheric Administration (NOAA) buoys (US 192 and US 430) off the North Carolina Shores. A predictive method was employed on the data and average wave heights and time periods were estimated for the above mentioned sites [39]. The stokes 5^{th} order wave is derived from solving the Laplace's equation [40]:

$$u = \frac{\partial \psi}{\partial y} \tag{3.13}$$

$$v = \frac{\partial \psi}{\partial x} \tag{3.14}$$

where ψ is the streamline function and u and v are the free-stream velocity components along x- and y- axis. For an irrotational motion, ψ satisfies the Laplace's equation throughout the fluid

$$\frac{\partial^2 \psi}{\partial y^2} + \frac{\partial^2 \psi}{\partial x^2} = 0 \tag{3.15}$$

On a free surface, applying the kinematic boundary condition on equation 3.15 gives

$$\frac{1}{2}[(\frac{\partial \psi}{\partial y})^2 + (\frac{\partial \psi}{\partial x})^2] + g\eta = R \tag{3.16}$$

where R is a positive constant denoting the total volume flow rate underneath the stationary wave per unit length and η is the instantaneous water depth [40].

The meshes for the simulations were created on StarCCM+ using the automated mesh feature. A trimmed cell mesh was used for the volume mesh and a volume refinement was performed for the interface between the air and water. Trimmed cell mesh provides a good quality of robustness and provides a high quality mesh for analysis of simple as well as complex problems. Most notable advantages of using trimmed cell mesh include [41]:

- predominantly hexahedral cells with minimum skewness.
- refinement based on surface mesh size and user-defined inputs.
- surface quality independency.
- alignment with user-specified coordinate system.

The surface mesh on the body was refined and also prism layer mesh was modelled to be able to capture the effects of turbulence accurately. 12 prism layers were modelled with a first layer thickness of 0.001 mm. The first prism layer thickness is pivotal in maintaining a wall y+ value within the acceptable range for solution accuracy.

The simulations were 3-D and the time scheme was an implicit unsteady scheme. 3-D simulation was chosen as it helps to capture the forces experienced by the whole body in all directions. The implicit scheme helps to increase the rate of convergence of solution as compared to an explicit scheme. Table 4.1 provides a complete overview of the physics setup.

Table 3.1: Physics models implemented

Group	Physics Model
Phase	3 Dimensional
Time	Implicit Unsteady
Material	Eulerian Multiphase Multiphase Interaction
Eulerian Multiphase	Volume of Fluid (VoF) Gradient Segregated Flow Multiphase Equation of State
Viscous Regime	Turbulent
Turbulence Model	Realizable k-ϵ and SST k-ω
Optional Model	Gravity VoF Waves

The Eulerian multiphase model solves the momentum, enthalpy, and continuity equations for each phase and tracks volume fractions. Also, since there is a free surface of water which is constantly deforming, the Lagrangian method cannot be used [42]. It also uses a single pressure field for all the phases. The advantages of the Eulerian model can be stated as the following [43]:

- Covers the full range of volume fractions (0-1).
- Mean quantities are obtained directly.

- is capable of modelling mixing and separation of phases.

The VoF method makes use of marker cells to indicate where the free surface lies (cells with volume fraction between 0-1) and enables the solver to identify the free surface and solve for the pressure field variation accordingly [42].

3.2.1 Challenges

There were different challenges in developing the CFD model. This Sub-Section reviews some of the major challenges and implemented solutions.

To reduce the computational cost, scaled models of the RM3 should be modeled. Hence, there is a risk in accurately setting up the computational domain to capture the wave motion effects accurately. To address this risk, different scaled-down models were studied and dimensional analysis were applied to the body, the domain and the wave characteristics.

To be able to capture the effects of the incident waves on the body, the cell size on the refinement area is kept to be at 40^{th} of the wavelength in the direction of wave propagation and 20^{th} of the wave height in the vertical direction. These guidelines were stated by International Towing Tank Conference and used as a starting point for the free surface refinement [44]. Also the surface mesh on the body is refined to help capture the hydrodynamic forces accurately. The size for this refinement is achieved by trial and error, where the surface mesh was refined up to a point where the force results between two meshes within the tolerance limits.

A slip wall boundary condition was set for the top boundary of the domain. This type of boundary condition reduces the computational time from that with a pressure outlet condition at the top. The slip wall boundary condition does not disturb the flow of fluid in the domain and instead acts as a pathway directing the flow of the fluid.

To prevent wave reflections into the domain, various methods such as creating a coarser mesh towards the outlet or using the inbuilt wave damping zone feature in

StarCCM+ were applied. In this study, the wave damping zone feature was utilized set at the outlet of the domain.

One of the most challenging aspects of this multi-phase problem, is the water-air interface meshing. An isosurface on the water surface was set-up to monitor the wave-height of the waves being simulated to establish if they are the same as those specified. The time-step for the simulation was chosen with respect to the wave time period and was set at 200^{th} of the wave time period.

At the ocean surface there is a momentum transfer from the wind to the water surface. The momentum enters first the surface wave field and then us transmitted to the surface current field mainly by wave breaking [45]. There is an increase in turbulent kinetic energy close to the sea surface and this is responsible for mixing of momentum down through the water, thus determining the shape of the near-surface current profile [46]. This calls for the need for a turbulence modelling technique. The Realizable $k-\epsilon$ model is able to capture the near wall effects in the boundary layer region and provide the free stream independent of $k-\epsilon$ model and the SST $k\omega$ model performs better in the near wall region; both these models were used in this study.

CHAPTER 4: RESULTS

4.1 WEC-Sim

The RM3 body geometry specifications and incident wave inputs were passed through the WAMIT BEM code. The hydrodynamic force coefficients were calculated. The force coefficients obtained from WAMIT is then used to run WEC-Sim and obtain the pitch and surge forces on the body and reaction of the body to these forces. The waves were generated by JONSWAP spectrum, which is widely used to model multi-directional waves. The spectral analysis provided a framework to decompose individual harmonics and helped understanding their behavior separately [47]. The RM3 body forces with respect to time are illustrated in figure 4.1 and 4.2. It is noted that for a ramp time of 100 seconds as chosen for the considerations of this simulation, the body response is gradually increasing. The fluctuation s seen are due to the non-linear behavior of the waves.

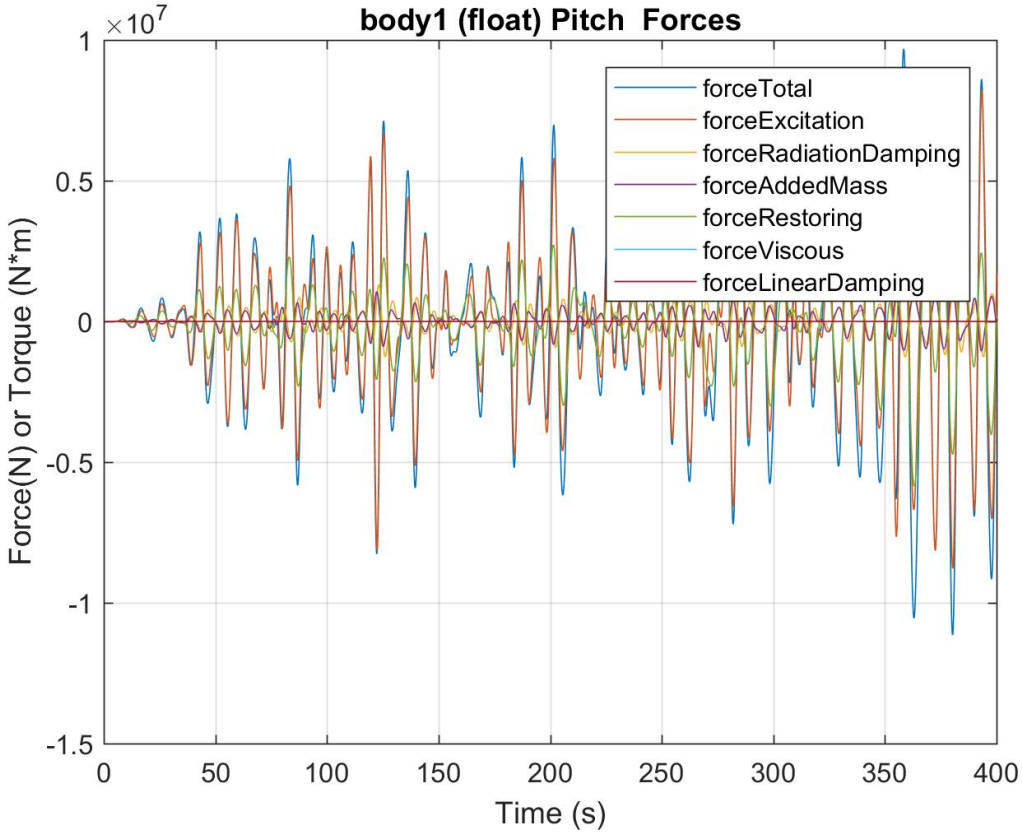

Figure 4.1: Pitch force on float [4]

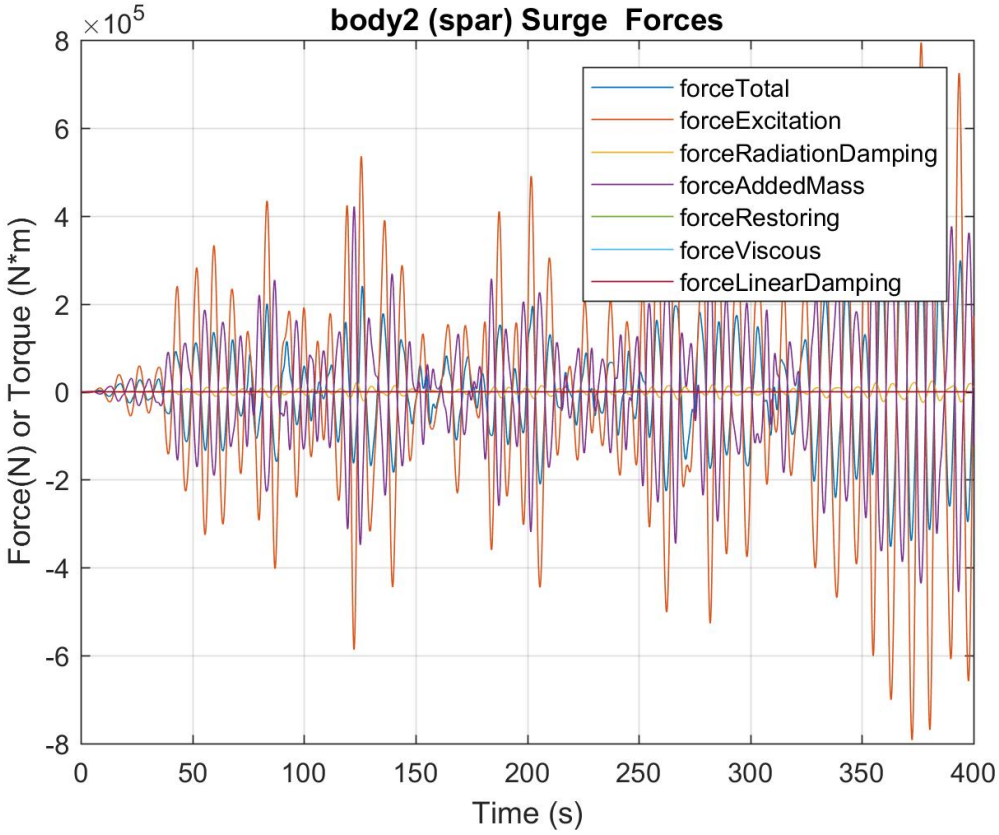

Figure 4.2: Surge force on spar [4]

From the heave and surge response of the float and spar, the total amount of wave force experienced by the body is estimated. The various forces which are calculated from the Cummins equation are the total force experienced by the body. The wave excitation forces, namely; buoyancy and non-linear Froude-Krylov forces account for close to 80% of the total force and are calculated by locating the position of each body and integrating the hydrostatic and hydrodynamic pressure force for each time step over the wetted body surface [48]. The radiation damping and added mass force account for the inaccuracies in calculating the wave excitation forces. The body responses to these forces show an expected behavior of having peaks at time with the high total pitch forces. The response of the float to the incident waves in pivotal in calculation of performance of the system.

4.2 Validation Case

The methodology for the validation case was followed as per the findings of Aidan et al. [38]. The CFD simulations were set-up and solved in StarCCM+. Figure 4.3 shows the volume mesh over the domain and figure 4.4 shows the mesh refinement on the free surface to capture the effects of the wave interaction on the body and the surface mesh on the body. The mesh skewness angle was found to be less than 80 which is a good measure to check for quality of mesh [49]. A mesh independency analysis was conducted for this case with mesh sizes varying from 2.8 million to 9.2 million cells. The variation of resultant force in x and y direction was found to be less than 2% between 7.2 million cells and 9.2 million cells; it was considered as a converging point for the mesh Independence analysis. This can be further seen in figure 4.5.

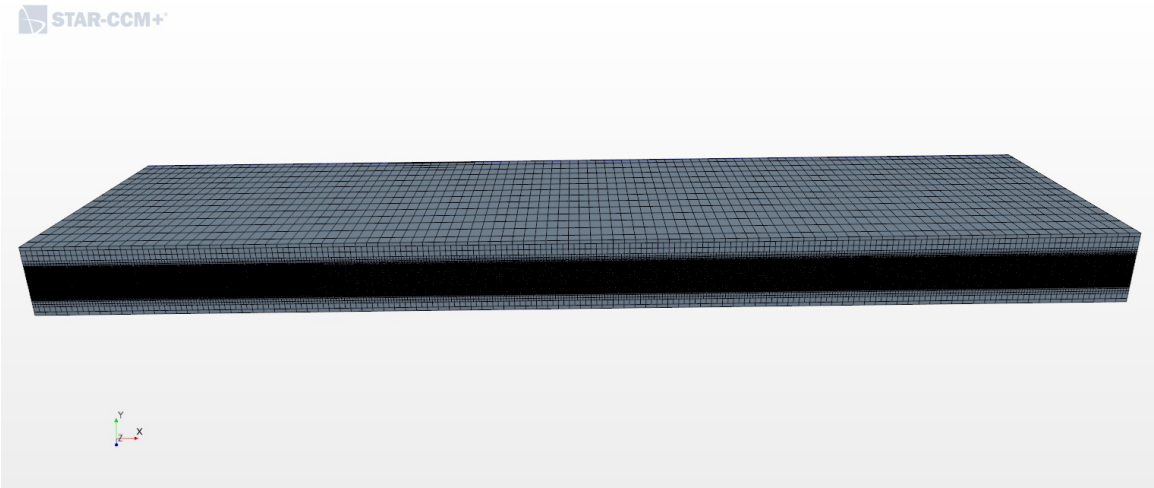

Figure 4.3: Volume mesh result on the studied computational domain

The X-direction force results were compared with those from Aidan et al. It was found the calculated forces were 3.5 times lower, but, followed a very similar trend as it can be seen in figure 4.6. This deviation in results was attributed to the pressure outlet boundary condition used by the reference as opposed to the slip wall boundary

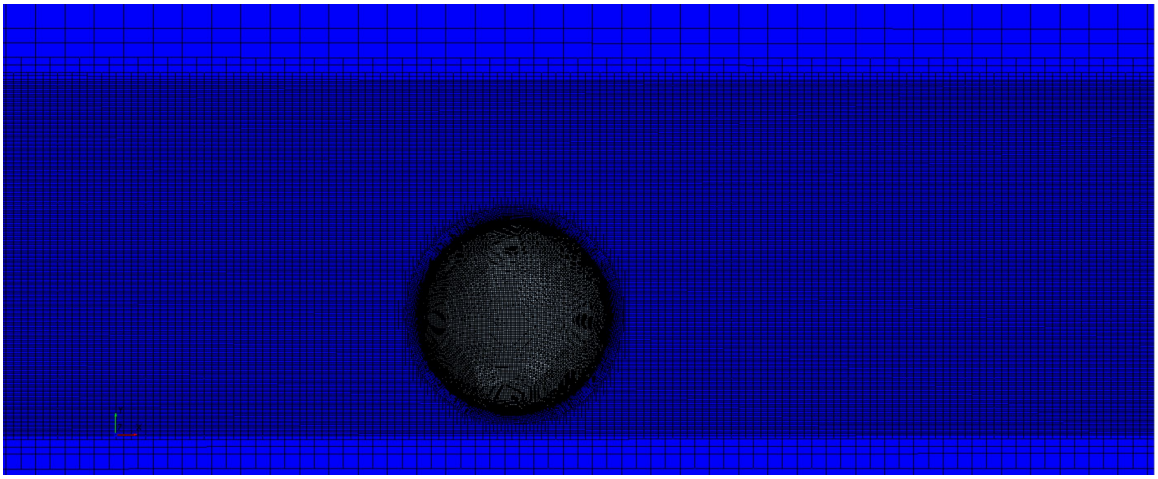

Figure 4.4: Mesh refinement at air-water interface

condition used in this study. This change in boundary condition was made to reduce the computational cost and eliminate the need for a finer mesh in the domain.

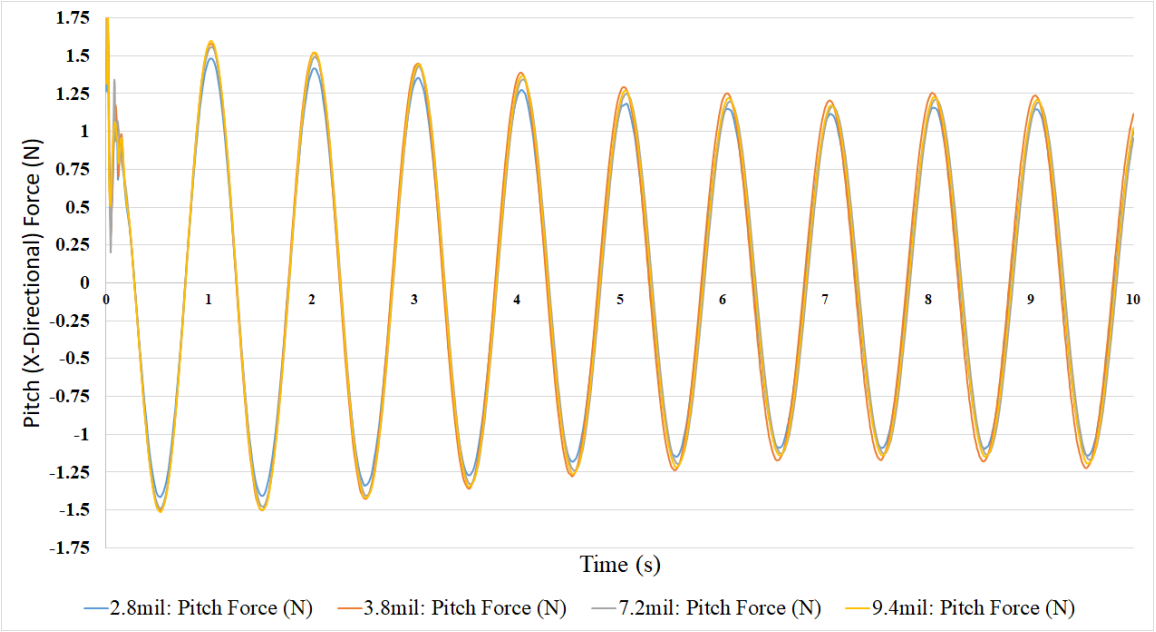

Figure 4.5: Mesh sensitivity analysis

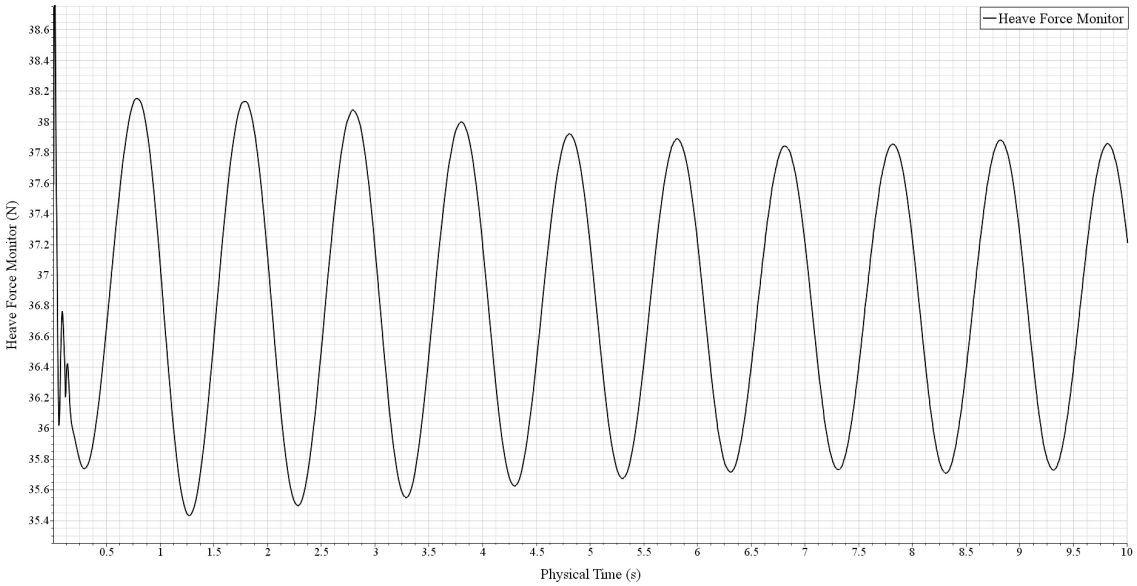

Figure 4.6: Heave force

The wall y+ scene showed values less than 5 throughout the sphere. This is illustrated in figure 4.7

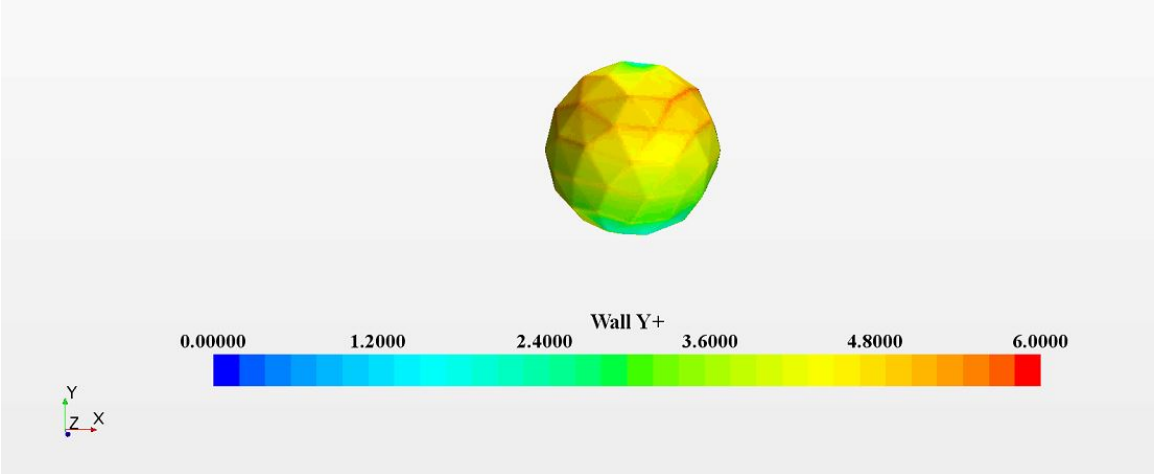

Figure 4.7: Wall y+ value for the sphere

4.3 Reference Model 3

The RM3 device was scaled to 50^{th}, 100^{th} and 200^{th} to be able to analyze their behavior accurately given the computational restrictions involved with the study. The scaled down dimensions for the model can be seen in the table 4.1.

Table 4.1: Scaled RM3 Dimensions

	Scaled 50^{th}	Scaled 100^{th}	Scaled 200^{th}
Float inner diameter (m)	0.12	0.6	0.3
Float outer diameter (m)	0.4	0.2	0.1
Spar length (m)	0.76	0.38	0.19

Mesh over the NWT for RM3 was created using the same methodology as that of the validation case. This can be better illustrated in figure 4.8.

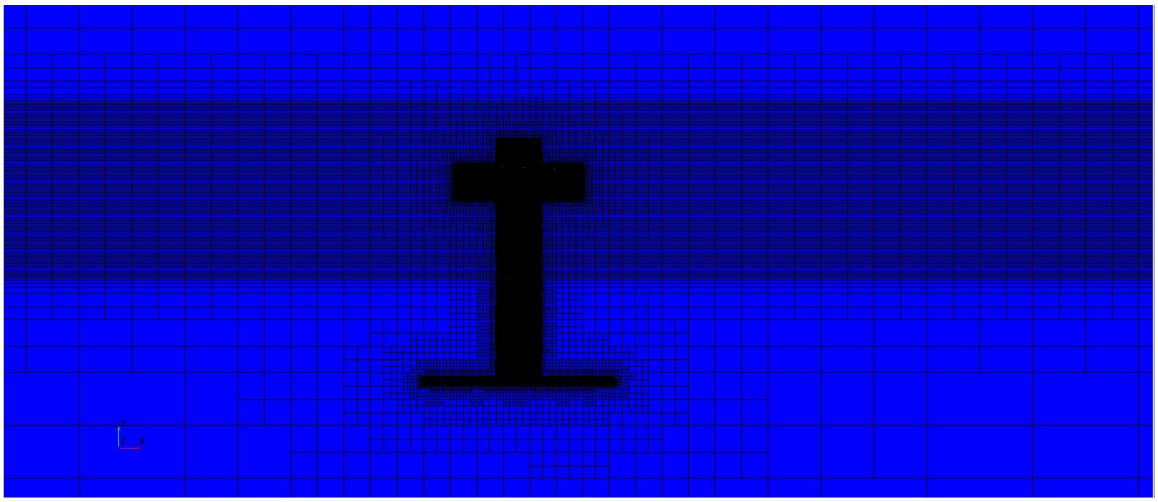

Figure 4.8: The mesh refinement along the free surface

To ensure there were no wave reflection in the NWT, the simulation was run for 20 seconds. The results show that there are no drastic changes in the forces, thus confirming that there are no wave reflections in the system.

The pitching forces on scaled 50^{th}, 100^{th}, and 200^{th} RM3 models are shown in figure 4.9, figure 4.10, and figure 4.11 respectively.

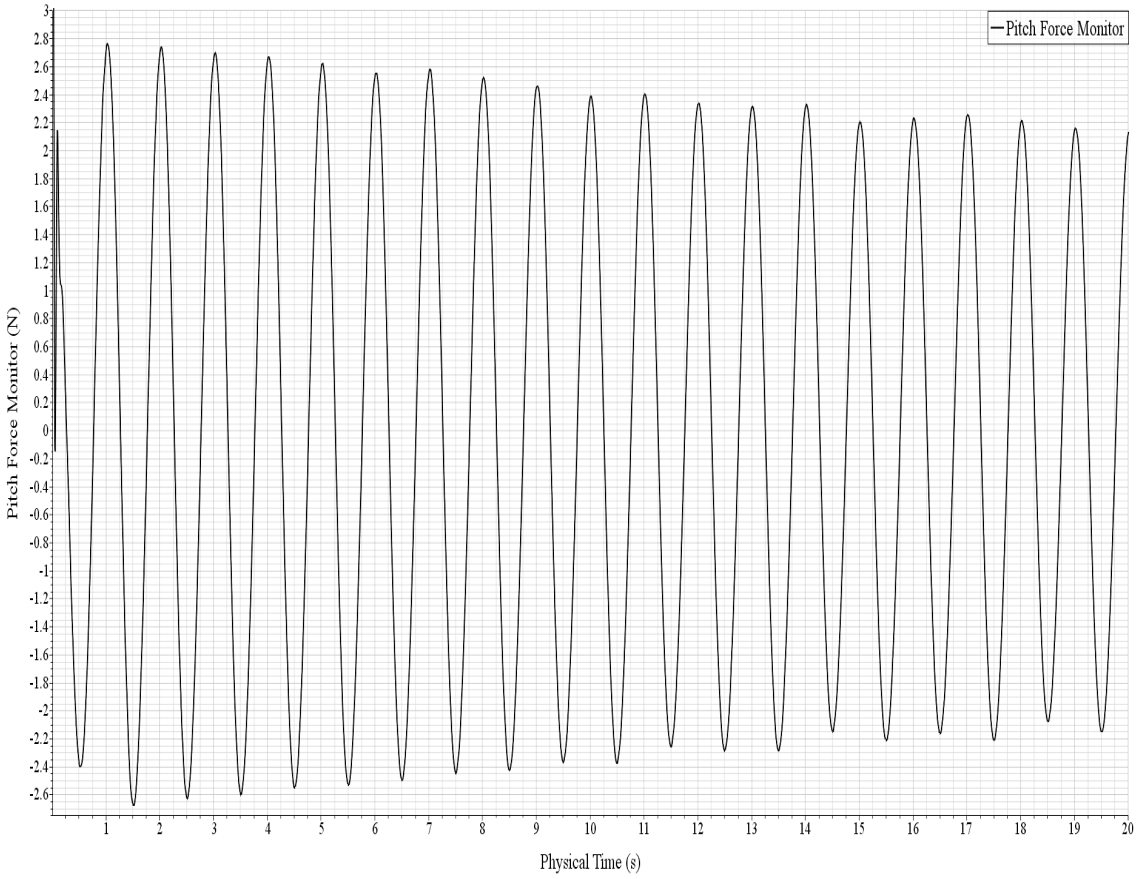

Figure 4.9: Pitch force on 50^{th} scaled RM3

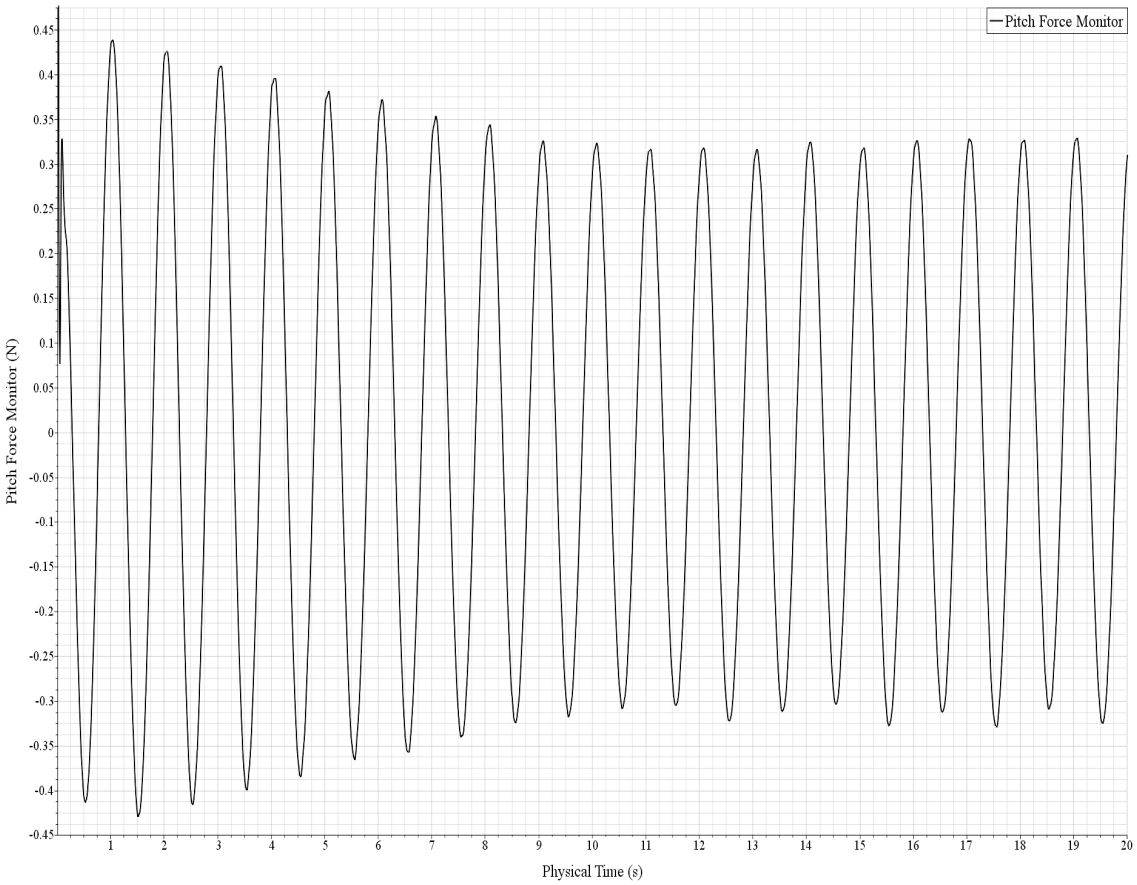

Figure 4.10: Pitch force on 100^{th} scaled RM3

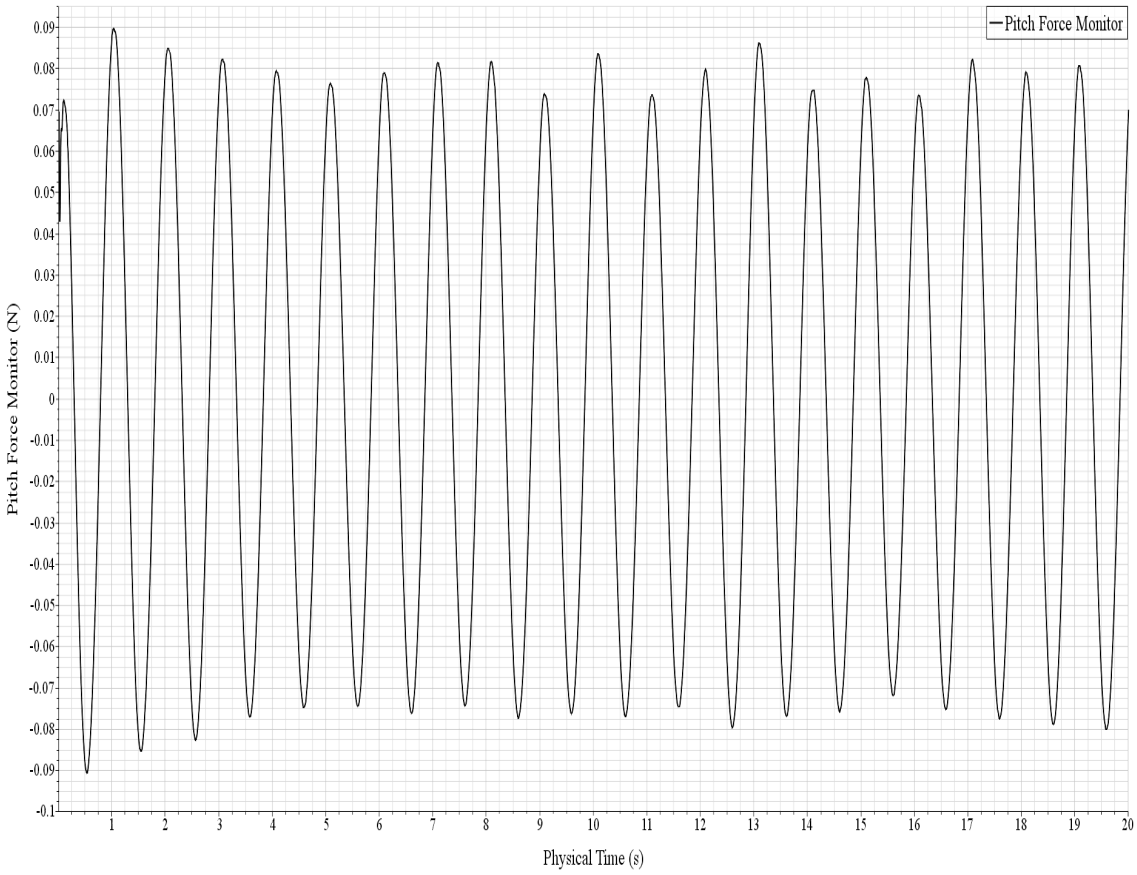

Figure 4.11: Pitch force on 200^{th} scaled RM3

The heave force on the device for each scaled model is shown in figure 4.12, figure 4.13, and figure 4.14 respectively.

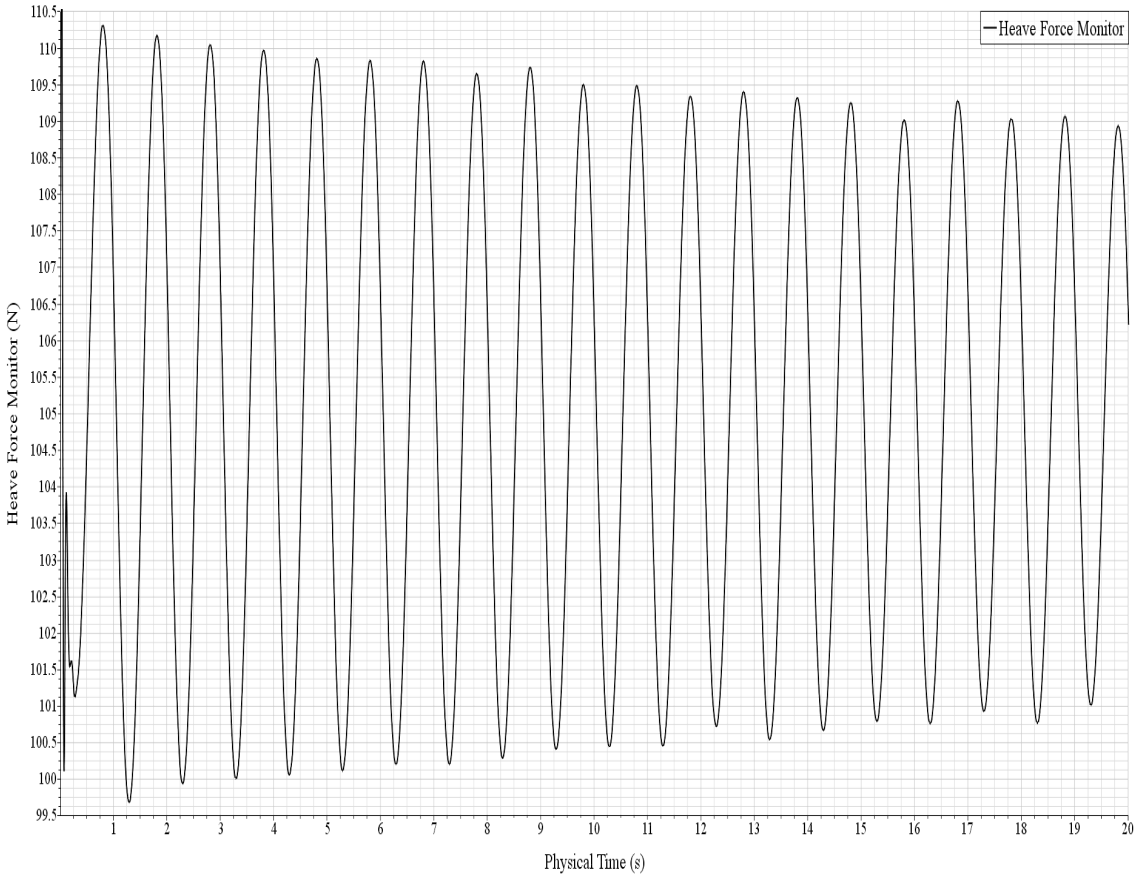

Figure 4.12: Heave force on 50^{th} scaled RM3

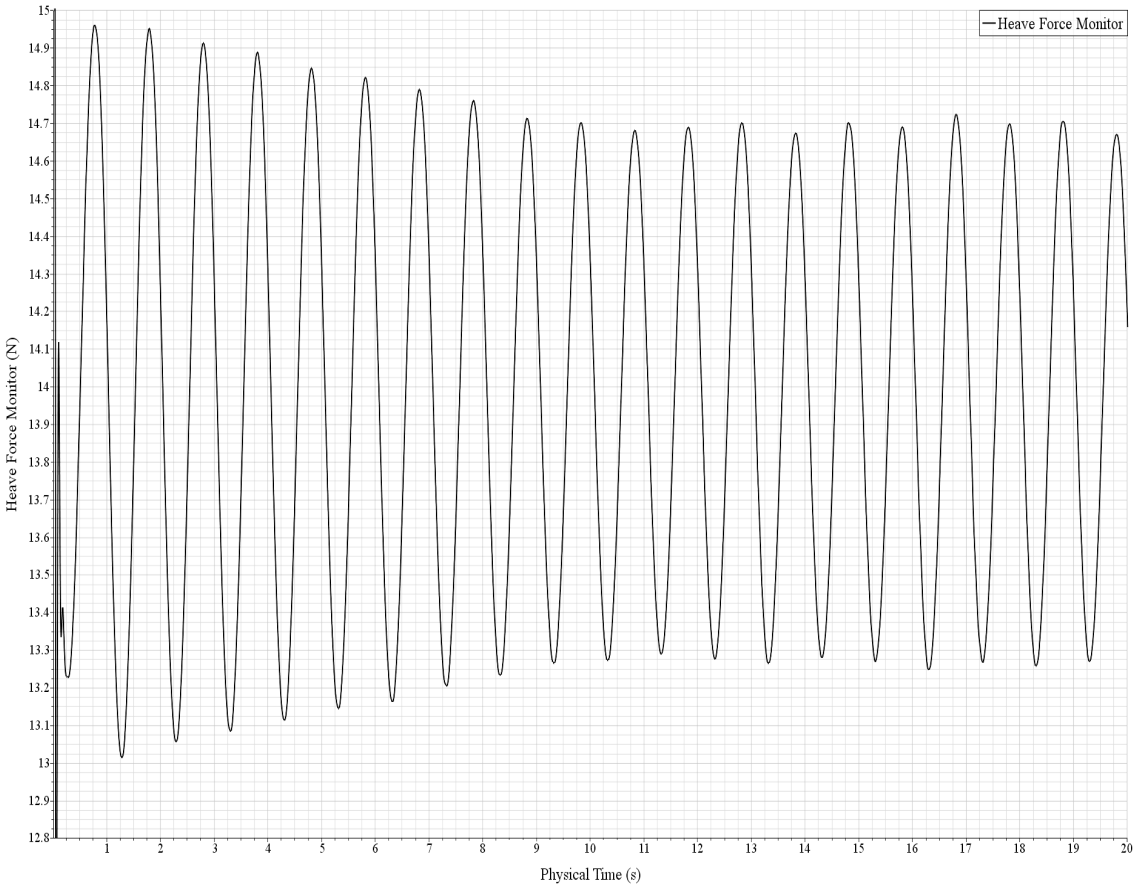

Figure 4.13: Heave force on 100^{th} scaled RM3

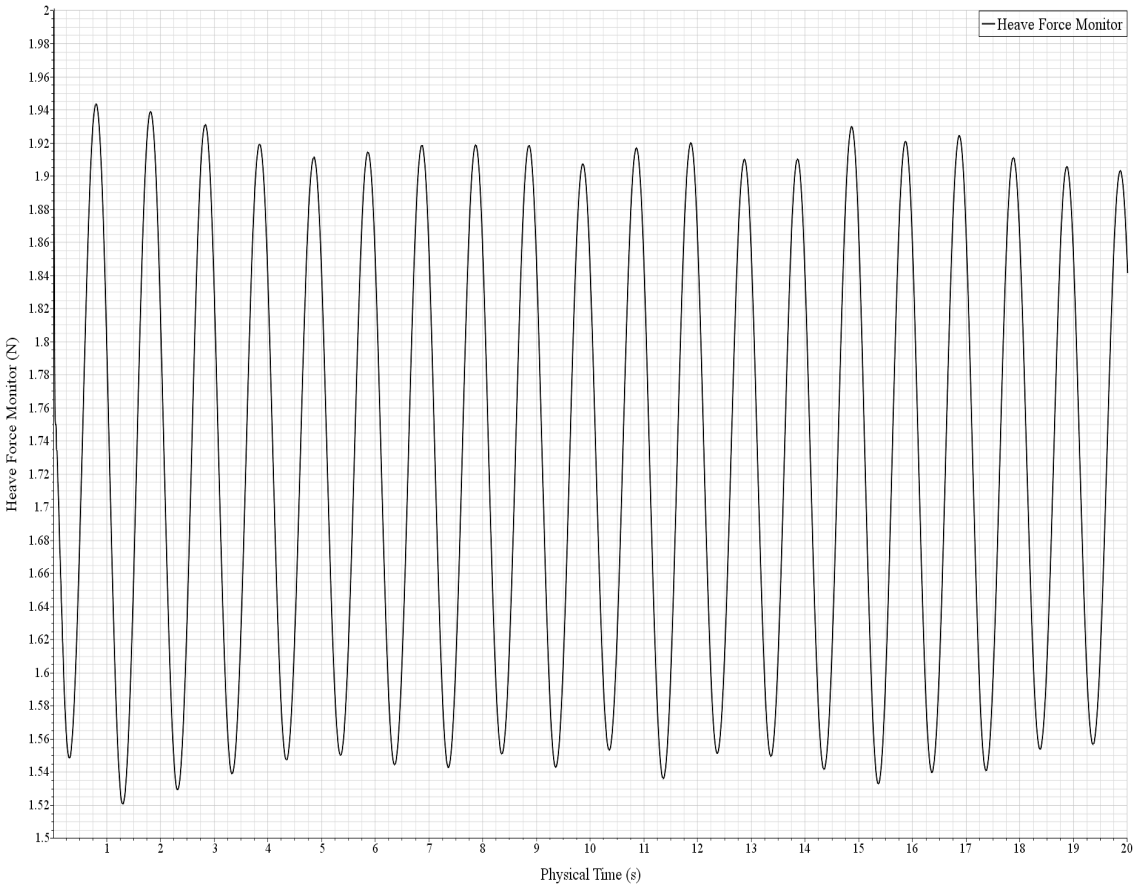

Figure 4.14: Heave force on 200^{th} scaled RM3

The sinusoidal behavior of the forces are due to those of the incident wave on the stationary body. Mesh independence analysis was carried out for each case with mesh sizing determined by the domain and scaled RM3 sizes. The sizes ranged from 3.3 million cells to 7.4 million cells for 50^{th} scaled model to 1.2 million cells to 3.6 million cells for 200^{th} scaled model.

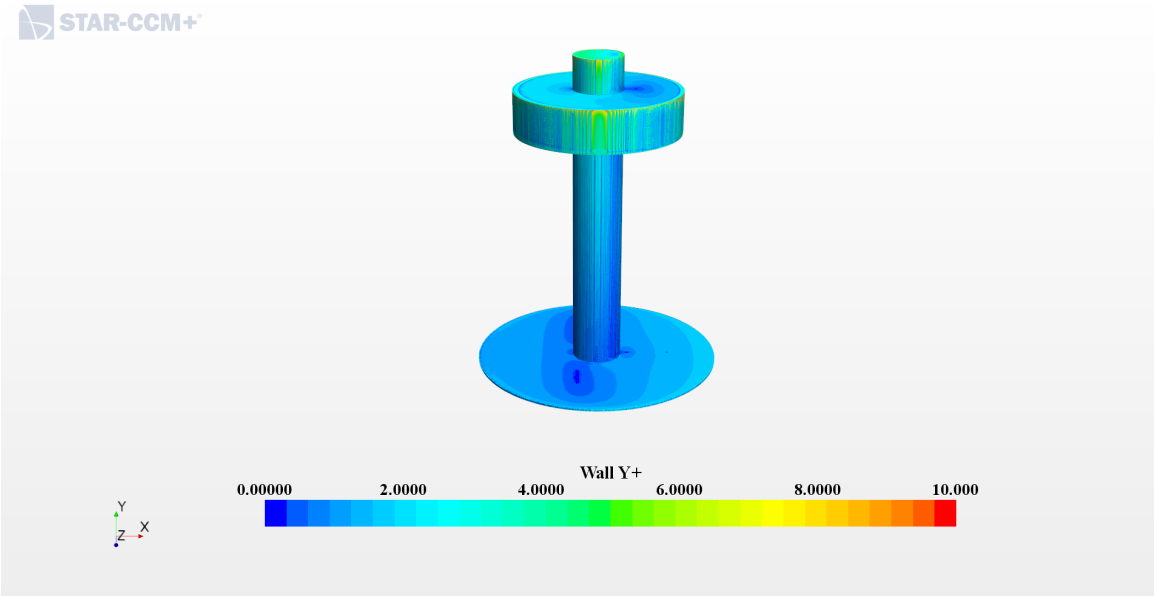

Figure 4.15: Wall Y+ over 50^{th} scaled RM3 model

The solution accuracy was checked with the wall y+ scene and consistency in forces was validated as seen in figure 4.15.

4.4 Conclusion

WEC-Sim helps the user to understand the hydrodynamic forces on a WEC device, but does not let one to tabulate the results and hence eliminates the chance of performing post-processing on the resultant forces. This major drawback minimizes the applicability of WEC-Sim. A CFD based approach helps to eliminate this drawback and it also gives a better understanding of the forces as it accounts for the turbulent behavior of incident waves; not simply solving for the Laplace equation.

The diffraction force results from this study completes half of the total hydrodynamic forces acting on the WEC device. The diffraction study combined with the radiation study would account for the total hydrodynamic force distribution on the RM3 model and the addition of these forces would help to assess the performance of the RM3 device. The pitch forces vary in x-direction and the heave forces vary in the y-direction. These also account for any mooring force acting on the system as the

movement of the device is constrained.

4.5 Future Scope

Future scope of this work would be studying the radiation forces from the sphere oscillating vertically in a still water. Subsequently, each case can be run with different turbulence models and the difference in force estimation for each turbulence model can be visualized. A water flume with the purpose of testing WEC prototypes was designed and validated along this thesis [50]. Water flumes promote relatively inexpensive prototype testing of contemporary designs for WEC devices which would in turn help moderate faster deployment of WEC devices.

Experimental prototype testing on scaled WEC devices can be performed along the North Carolina shore using the wave heights and time periods as those in the simulations are derived from NOAA buoys data. Once the size of the prototype for experimental testing is determined, using dimensional analysis utilized in this study, the site characteristics for the testing can be determined; the vice-versa approach is doable too. As a part of another ongoing project at NADGOD research group, a wave tank with 0.5 m depth, 3.5 m length and 1 m width is under construction. The scaled RM3 prototype has the following dimensions: float diameter of 0.0625 m and thickness of 0.015 m, the spar length of 0.125 m and a diameter of 0.018 m. Wave heights of 30 mm and a time period of 1 s will be generated. The experimental data from this test will be pivotal in validating the CFD results from this study.

REFERENCES

[1] "Public data from Environmental Protection Agency," 2016. [Online; accessed 23-November-2018].

[2] R. So, A. Simmons, T. Brekken, K. Ruehl, and C. Michelen, "Development of pto-sim: A power performance module for the open-source wave energy converter code wec-sim," in *ASME 2015 34th International Conference on Ocean, Offshore and Arctic Engineering*, pp. V009T09A032–V009T09A032, American Society of Mechanical Engineers, 2015.

[3] "Public data from Department of Energy - Wave Energy Converter Simulator,"

[4] A. Subramanian, G. Raut, and N. Goudarzi, "Integration of wave energy harnessing technologies to the needs of coastal societies in north carolina," in *ASME 2018 Power and Energy Conference*, American Society of Mechanical Engineers, 2018.

[5] V. S. Neary, M. Lawson, M. Previsic, A. Copping, K. C. Hallett, A. LaBonte, J. Rieks, and D. Murray, "Methodology for design and economic analysis of marine energy conversion (mec) technologies.," tech. rep., Sandia National Lab.(SNL-NM), Albuquerque, NM (United States), 2014.

[6] S. Bozzi, G. Besio, and G. Passoni, "Wave power technologies for the mediterranean offshore: Scaling and performance analysis," *Coastal Engineering*, vol. 136, pp. 130–146, 2018.

[7] F. Birol, "Energy efficiency," 2017.

[8] J. L. Sawin, E. Martinot, V. Sonntag-O'Brien, A. McCrone, J. Roussell, D. Barnes, C. Flavin, L. Mastny, D. Kraft, S. Wang, *et al.*, "Renewables 2017-global status report," 2017.

[9] "Public data from Department of Energy," 2017. [Online; accessed 30-November-2018].

[10] "Public data from Energy Information Administration," 2017. [Online; accessed 28-November-2018].

[11] "Public data from Office of Energy Efficiency and Renewable Energy," 2017. [Online; accessed 1-December-2018].

[12] K. M. Ruehl, C. Michelen, Y.-H. Yu, and M. Lawson, "Development and demonstration of the wec–sim wave energy converter simulation tool.," tech. rep., Sandia National Lab.(SNL-NM), Albuquerque, NM (United States), 2014.

[13] A. Poullikkas, "Technology prospects of wave power systems," *Electronic Journal of Energy & Environment*, vol. 2, no. 1, pp. 47–69, 2014.

[14] "Public data from Archimedes Waveswing," 2016. [Online; accessed 23-July-2018].

[15] "Public data from Langlee Wave Power," 2013. [Online; accessed 23-July-2018].

[16] "Public data from Pelamis Wave Power," 2011. [Online; accessed 27-July-2018].

[17] S. Sirnivas, Y.-H. Yu, M. Hall, and B. Bosma, "Coupled mooring analyses for the wec-sim wave energy converter design tool," in *ASME 2016 35th International Conference on Ocean, Offshore and Arctic Engineering*, pp. V006T09A023–V006T09A023, American Society of Mechanical Engineers, 2016.

[18] W. Finnegan and J. Goggins, "Numerical simulation of linear water waves and wave–structure interaction," *Ocean Engineering*, vol. 43, pp. 23–31, 2012.

[19] G. Wu and Z. Hu, "Simulation of nonlinear interactions between waves and floating bodies through a finite-element-based numerical tank," in *Proceedings of the Royal Society of London A: Mathematical, Physical and Engineering Sciences*, vol. 460, pp. 2797–2817, The Royal Society, 2004.

[20] I. Hadžić, J. Hennig, M. Perić, and Y. Xing-Kaeding, "Computation of flow-induced motion of floating bodies," *Applied mathematical modelling*, vol. 29, no. 12, pp. 1196–1210, 2005.

[21] E. B. Agamloh, A. K. Wallace, and A. Von Jouanne, "Application of fluid–structure interaction simulation of an ocean wave energy extraction device," *Renewable Energy*, vol. 33, no. 4, pp. 748–757, 2008.

[22] G. Raut and N. Goudarzi, "North carolina wave energy resource: Hydrogen production potential.," in *ASME 2018 Power and Energy Conference*, American Society of Mechanical Engineers, 2018.

[23] J. Journée and W. Massie, *Offshore Hydromechanics*. 2001.

[24] J. Wheeler *et al.*, "Methods for calculating forces produced by irregular waves," in *Offshore technology conference*, Offshore Technology Conference, 1969.

[25] J. Morison, J. Johnson, S. Schaaf, *et al.*, "The force exerted by surface waves on piles," *Journal of Petroleum Technology*, vol. 2, no. 05, pp. 149–154, 1950.

[26] B. Teng and R. E. Taylor, "New higher-order boundary element methods for wave diffraction/radiation," *Applied Ocean Research*, vol. 17, no. 2, pp. 71–77, 1995.

[27] E. A. Salgado-Ibarra, "Boundary Element Method (BEM) and method of fundamental solutions (mfs) for the boundary value problems of the 2-d laplace's equation," 2011.

[28] Y. Liu, C. Kim, X. Lu, *et al.*, "Comparison of higher-order boundary element and constant panel methods for hydrodynamic loadings," in *The First ISOPE European Offshore Mechanics Symposium*, International Society of Offshore and Polar Engineers, 1990.

[29] Y. Liu, C. Kim, M. Kim, *et al.*, "The computation of mean drift forces and wave run-up by higher-order boundary element method," in *The First International Offshore and Polar Engineering Conference*, International Society of Offshore and Polar Engineers, 1991.

[30] R. E. Taylor and F. Chau, "Wave diffraction theory-some developments in linear and nonlinear theory," *Journal of Offshore Mechanics and Arctic Engineering*, vol. 114, no. 3, pp. 185–194, 1992.

[31] R. E. Taylor, B. Teng, *et al.*, "The effect of corners on diffraction/radiation forces and wave drift damping," in *Offshore Technology Conference*, Offshore Technology Conference, 1993.

[32] B. Teng and Y. Gou, "Bem for wave interaction with structures and low storage accelerated methods for large scale computation," *Journal of Hydrodynamics, Ser. B*, vol. 29, no. 5, pp. 748–762, 2017.

[33] *Wamit 7.2 User's Guide.*

[34] J. Cornthwaite, "Pressure poisson method for the incompressible navier-stokes equations using galerkin finite elements," 2013.

[35] J. Wu, "Froude number scaling of wind-stress coefficients," *Journal of the Atmospheric Sciences*, vol. 26, no. 3, pp. 408–413, 1969.

[36] S. A. Hughes, *Physical models and laboratory techniques in coastal engineering*, vol. 7. World Scientific, 1993.

[37] J. Wu, "The sea surface is aerodynamically rough even under light winds," *Boundary-Layer Meteorology*, vol. 69, no. 1-2, pp. 149–158, 1994.

[38] A. Bharath, J.-R. Nader, I. Penesis, and G. Macfarlane, "Nonlinear hydrodynamic effects on a generic spherical wave energy converter," *Renewable Energy*, vol. 118, pp. 56–70, 2018.

[39] G. Raut, "Technical analysis of hydrogen production from wave energy: A case study for North Carolina," Master's thesis, University of North Carolina Charlotte, 9201 University City Blvd., Charlotte, North Carolina, 28223, 2018.

[40] J. D. Fenton, "A fifth-order stokes theory for steady waves," *Journal of waterway, port, coastal, and ocean engineering*, vol. 111, no. 2, pp. 216–234, 1985.

[41] *StarCCM+ 11.06 User's Guide.*

[42] C. W. Hirt and B. D. Nichols, "Volume of fluid (vof) method for the dynamics of free boundaries," *Journal of computational physics*, vol. 39, no. 1, pp. 201–225, 1981.

[43] H.-J. Kim, "Multiphase modelling in starccm+," 2012.

[44] "Ittc, international towing tank conference recommended procedures and guidelines - cfd users guide," tech. rep., International Towing Tank Conference, 1999.

[45] Phillips and M. Owen, *The Dynamics of the Upper Ocean*. Cambridge university press, 1977.

[46] W. Drennan, K. Kahma, E. Terray, M. Donelan, and S. Kitaigorodskii, "Observations of the enhancement of kinetic energy dissipation beneath breaking wind waves," in *Breaking waves*, pp. 95–101, Springer, 1992.

[47] "Public data from Overview of ocean wave statistics," 2014. [Online; accessed 19-March-2018].

[48] M. Lawson, Y.-H. Yu, A. Nelessen, K. Ruehl, and C. Michelen, "Implementing nonlinear buoyancy and excitation forces in the wec-sim wave energy converter modeling tool," in *ASME 2014 33rd International Conference on Ocean, Offshore and Arctic Engineering*, pp. V09BT09A043–V09BT09A043, American Society of Mechanical Engineers, 2014.

[49] A.-C. Bayeul-Laine, P. Dupont, G. Cavazzini, A. Dazin, P. Cherdieu, G. Bois, and O. Roussette, "Investigations in a vaned difuser of shf impeller," 2013.

[50] A. Subramanian and N. Goudarzi, "CFD analysis of a water flume design for testing marine and hydrokinetics energy converters," in *ASME 2018 Power and Energy Conference*, American Society of Mechanical Engineers, 2018.

APPENDIX A: StarCCM+

Summary Report: Diffraction_exact_top_walll_11_2.8mil

Session Summary

Date	Oct 12, 2018 6:02:33 PM
Simulation	D:\AKSHITH\Akshith\Paper_WEC\Diffraction_exact_top_walll_11_2.8mil.sim
File size	1.1e+03 MB
Number of Partitions	8
Number of Restored Partitions	16

Software Summary

Version	BuildArch: win64 BuildEnv: intel15.0 ReleaseDate: Thu Nov 10 20:49:47 UTC 2016 ReleaseNumber: 11.06.011
MPI Version	Platform Computing MPI-9.1.4.2

Hardware Summary

Hosts	Number Processes: 8 Rank[0]: COE-DYSJHH2 Rank[1]: COE-DYSJHH2 Rank[2]: COE-DYSJHH2 Rank[3]: COE-DYSJHH2 Rank[4]: COE-DYSJHH2 Rank[5]: COE-DYSJHH2 Rank[6]: COE-DYSJHH2 Rank[7]: COE-DYSJHH2

Simulation Properties

1 **Diffraction_exact_top_walll_11_2.8mil**		
+-1 Contacts		
+-2 3D-CAD Models		
| `-1 **3D-CAD Model 1**	Tags	[]
| +-1 Bodies		
| | `-1 **Body 1**		
| +-2 Features		
| | +-1 **XY**	Error Message	
| | |	Origin	[0.0, 0.0, 0.0] m
| | |	X-Axis	[1.0, 0.0, 0.0]
| | |	Y-Axis	[0.0, 1.0, 0.0]
| | |	Tags	[]
| | +-2 **YZ**	Error Message	
| | |	Origin	[0.0, 0.0, 0.0] m
| | |	X-Axis	[0.0, 1.0, 0.0]
| | |	Y-Axis	[0.0, 0.0, 1.0]
| | |	Tags	[]
| | +-3 **ZX**	Error Message	
| | |	Origin	[0.0, 0.0, 0.0] m
| | |	X-Axis	[0.0, 0.0, 1.0]
| | |	Y-Axis	[1.0, 0.0, 0.0]
| | |	Tags	[]
| | +-4 **Global Origin**	Error Message	
| | |	Position	[0.0, 0.0, 0.0]
| | |	Tags	[]
| | +-5 **Lab Coordinate System**	Error Message	
| | |	Origin	[0.0, 0.0, 0.0]

```
|   `-3 Design Parameters
+-3 Parts
| +-1 Block
| | | |
| | | |
| | | |
| | | |
| | | |
| | | |
| | | |
| | | |
| | +-1 Surfaces
| | | +-1 bottom
| | | | |
| | | | |
| | | | |
| | | +-2 far_feild
| | | | |
| | | | |
| | | | |
| | | +-3 inlet
| | | | |
| | | | |
| | | | |
| | | +-4 outlet
| | | | |
| | | | |
| | | | |
| | | +-5 symmetry_plane
| | | | |
| | | | |
| | | | |
| | | `-6 top
| | | |
| | | |
| | | |
| | `-2 Curves
| |   `-1 Block Curve
| | |
| | |
| +-2 Block 2
| | | |
| | | |
| | | |
| | | |
| | | |
| | | |
| | | |
| | | |
| | | |
| | +-1 Surfaces
```

Metadata	{}
Index	2
Region	[]
Contacts	[]
Descriptions	[Root]
Face Count	12
Coordinate System	Laboratory
Corner 1	[-5.0, -0.395, 0.0] m,m,m
Corner 2	[10.0, 0.605, 4.0] m,m,m
Tags	[]

Metadata	{}
Index	10
Boundary	[]
Tags	[]
Metadata	{}
Index	8
Boundary	[]
Tags	[]
Metadata	{}
Index	6
Boundary	[]
Tags	[]
Metadata	{}
Index	9
Boundary	[]
Tags	[]
Metadata	{}
Index	7
Boundary	[]
Tags	[]
Metadata	{}
Index	2
Boundary	[]
Tags	[]

Feature Curve	[]
Index	1
Tags	[]
Metadata	{}
Index	3
Region	[]
Contacts	[]
Descriptions	[Root]
Face Count	12
Coordinate System	Laboratory
Corner 1	[-5.0, -0.15000000000000002, 0.0] m,m,m
Corner 2	[10.0, 0.3, 4.0] m,m,m
Tags	[]

`-1 **Block Surface**	
	Metadata {}
	Index 3
	Boundary []
	Tags []
`-2 Curves	
`-1 **Block Curve**	
	Feature Curve []
	Index 2
	Tags []
+-3 **Body 1**	Metadata {}
	Index 1
	Region []
	Contacts []
	Descriptions [Root]
	Face Count 9408
	Tags []
+-1 Surfaces	
`-1 **Default**	
	Metadata {}
	Index 1
	Boundary []
	Tags []
`-2 Curves	
`-4 **Subtract**	
	Metadata {}
	Index 4
	Region [Region]
	Contacts []
	Descriptions [Root, Automated Mesh.Remesh]
	Face Count 4816
	Operation Subtract
	Tags []
+-4 Operations	
+-1 **Subtract**	
	Perform CAD Boolean false
	Input Parts [Block, Body 1]
	Target Part [Block]
	Output Parts [Subtract]
	Tags []
`-1 Remesh Intersection Curve	Remesh Intersection Curve false
`-2 **Automated Mesh**	Per-Part Meshing false
	Mesher Execution Mode Parallel
	Input Parts [Subtract]
	Perform Local Surface Meshing false
	Preserve Surface Perimeters None
	Verbose Output false
	Tags []
+-1 Meshers	
+-1 Surface Remesher	Perform Curvature Refinement true
	Perform Proximity Refinement true
	Perform Compatibility Refinement false
	Create Aligned Meshes true
	Minimum Face Quality 0.05
+-2 Automatic Surface Repair	Connected Surface Count Limit None
	Connected Surface Size Limit(s) None
	Minimum Face Quality 0.05
+-3 Trimmed Cell Mesher	Core Cell Type Hexahedra
	Coordinate System Laboratory
	Perform Mesh Alignment false
	Size Dependent Growth All cells

10/12/2018 Diffraction_exact_top_walll_11_2.8mil

Rates	
Run Optimizer	true
Stretching Function	Geometric Progression
Distribution Mode	Wall Thickness
Boundary March Angle	50.0
Gap Fill Percentage	25.0
Minimum Thickness Percentage	10.0
Layer Reduction Percentage	50.0
Concave Angle Limit	0.0
Convex Angle Limit	360.0
Near Core Layer Aspect Ratio	0.0

Value	0.5 m
Project to CAD	true
Size Type	Relative to base
Percentage of Base	90.0
Absolute Size	0.45 m
Size Type	Relative to base
Percentage of Base	10.0
Absolute Size	0.05 m
Enable Curvature Deviation Distance	false
# Pts/circle	36.0
Search Floor	0.0 m
# Points in gap	2.0
Enable Search Ceiling	false
Surface Growth Rate	1.3
Minimum Proximity	0.01
Number of Prism Layers	10
Value	0.001 m
Size Type	Absolute
Value	0.015 m
Limit Cell Size by Prism Layer Thickness	false
Default Growth Rate	Fast
Surface Growth Rate	Disable
Size Type	Relative to base
Percentage of Base	10000.0
Absolute Size	50.0 m

Enable Control	Enabled
Controls Display Mode	All
Part Surfaces	[Subtract.Block, Subtract.Block.bottom, Subtract.Block.far_feild, Subtract.Block.inlet, Subtract.Block.outlet, Subtract.Block.top]
Apply Only to Contacting Area	Disabled
Tags	[]

Target Surface Size	Parent
Minimum Surface Size	Parent
Curvature	Parent
Proximity	Parent
Proximity	Parent
Surface Growth Rate	Parent
Surface Remeshing	Parent
Prism Layers	Disable

+-9 Trimmer Surface Growth Rate	Trimmer Surface Growth Rate: Parent
+-10 Remesher Wake Refinement	Specify wake refinement options: Disabled
`-11 Trimmer Wake Refinement	Specify Trimmer Wake Refinement Options: Disabled
`-2 Values	
+-2 **Surface Control 2**	Enable Control: Enabled
	Controls Display Mode: All
	Part Surfaces: [Subtract.Body 1, Subtract.Body 1.Default]
	Apply Only to Contacting Area: Disabled
	Tags: []
+-1 Controls	
+-1 Target Surface Size	Target Surface Size: Custom
+-2 Minimum Surface Size	Minimum Surface Size: Custom
+-3 Surface Curvature	Curvature: Parent
+-4 Surface Proximity	Proximity: Parent
+-5 Edge Proximity	Proximity: Parent
+-6 Surface Growth Rate	Surface Growth Rate: Parent
+-7 Surface Remeshing	Surface Remeshing: Parent
+-8 Prism Layers	Prism Layers: Parent
+-9 Trimmer Surface Growth Rate	Trimmer Surface Growth Rate: Parent
+-10 Remesher Wake Refinement	Specify wake refinement options: Disabled
`-11 Trimmer Wake Refinement	Specify Trimmer Wake Refinement Options: Disabled
`-2 Values	
+-1 Target Surface Size	Size Type: Relative to base
`-1 Relative Size	Percentage of Base: 50.0
	Absolute Size: 0.25 m
`-2 Minimum Surface Size	Size Type: Relative to base
`-1 Relative Size	Percentage of Base: 10.0
	Absolute Size: 0.05 m
`-3 **Volumetric Control**	Enable Control: Enabled
	Controls Display Mode: All
	Parts: [Block 2]
	Tags: []
+-1 Controls	
+-1 Surface Remesher	Customize Size: Disabled
+-2 Prism Layer Mesher	Customize Number of Layers: Disabled
	Customize Total Thickness: Disabled
	Customize Stretching: Disabled
`-3 Trimmer	Customize Isotropic Size: Disabled
	Customize Anisotropic Size: Enabled
`-2 Values	
`-1 Trimmer Anisotropic Size	Relative/Absolute: Absolute
	Custom X Size: Enabled
	Custom Y Size: Enabled
	Custom Z Size: Enabled
+-1 Absolute X Size	Value: 0.015 m
+-2 Absolute Y Size	Value: 0.00375 m
`-3 Absolute Z Size	Value: 0.25 m
+-5 Descriptions	Number of Children: 3
+-1 Root	Described Parts: [Body 1, Block, Block 2, Subtract]
+-2 Automated Mesh.Remesh	Described Parts: [Subtract]
	Faces: 2152
	Vertices: 1078
`-3 Latest	Described Parts: [Body 1, Block, Block 2, Subtract]
	Faces: 11584
	Vertices: 5800

10/12/2018 Diffraction_exact_top_walll_11_2.8mil

+-6 Continua	Continua	2
| +-1 **Parts Meshes**	Interpolation Option	Nearest neighbor
| |	Regions	[Region]
| |	Interfaces	[]
| |	Tags	[]
| `-2 **Physics 1**	Regions	[Region]
| |	Interfaces	[]
| |	Point Sets	[]
| |	Active	true
| |	Tags	[]
| +-1 Models		
| | +-1 Eulerian Multiphase		
| | | +-1 Eulerian Phases		
| | | | +-1 **air**	Index	1
| | | | | `-1 Models		
| | | | | +-1 Constant Density		
| | | | | +-2 Gas		
| | | | | | `-1 **Air**	Database Material	Air (Air) [Standard/Gases]
| | | | | | | Tags	[]
| | | | | | | `-1 Material Properties		
| | | | | | | +-1 Density	Method	Constant
| | | | | | | | `-1 Constant	Value	1.18415 kg/m^3
| | | | | | | `-2 Dynamic Viscosity	Method	Constant
| | | | | | | | `-1 Constant	Value	1.85508E-5 Pa-s
| | | | | | `-3 Turbulent		
| | | | `-2 **water**	Index	2
| | | | | `-1 Models		
| | | | | +-1 Constant Density		
| | | | | +-2 Liquid		
| | | | | | `-1 **H2O**	Database Material	H2O (Water) [Standard/Liquids]
| | | | | | | Tags	[]
| | | | | | | `-1 Material Properties		
| | | | | | | +-1 Density	Method	Constant
| | | | | | | | `-1 Constant	Value	997.561 kg/m^3
| | | | | | | `-2 Dynamic Viscosity	Method	Constant
| | | | | | | | `-1 Constant	Value	8.8871E-4 Pa-s
| | | | | `-3 Turbulent		
| | | `-2 **Mixture**	Tags	[]
| | | | `-1 Material Properties		
| | | | `-1 Dynamic Viscosity	Method	Volume-Weighted Mixture
| | | | | `-1 Volume-Weighted Mixture		
| | +-2 Exact Wall Distance		
| | +-3 Gradients	Gradient Method	Hybrid Gauss-LSQ
| | |	Limiter Method	Venkatakrishnan
| | |	Custom Accuracy Level Selector	2.0
| | |	Verbose	false
| | |	Least-Squares Quality Criterion	true
| | |	Flat Cells Curvature Criterion	true
| | |	Cell Skewness Criterion	true
| | |	Chevron-Cell Criterion	true
| | |	Least-Squares Tensor Minimum Eigenvalues Ratio	0.1
| | |	Normalized Flat Cells Curvature Factor	1.0
| | |	Maximum Safe (Positive) Skewness Angle (deg)	75.0
| | |	Minimum Unsafe (Positive) Skewness Angle (deg)	88.0
| | |	Use TVB Gradient Limiting	false

(Factor)	
+-4 Gravity	
+-5 Implicit Unsteady	
+-6 K-Epsilon Turbulence	
+-7 Multiphase Equation of State	
+-8 Multiphase Interaction	
| `-1 Phase Interactions	
+-9 Realizable K-Epsilon Two-Layer	Buoyancy Production of Dissipation: Boundary Layer Orientation
	Cmu: 0.09
	C1e: 1.44
	C2e: 1.9
	Ct: 1.0
	Sigma_k: 1.0
	Sigma_e: 1.2
	Sarkar: 2.0
	Tke Minimum: 1.0E-10
	Tdr Minimum: 1.0E-10
	Secondary Gradients: On
	Convection: 2nd-order
	Normal Stress Term: false
	Curvature Correction Option: Off
	Two-Layer Type: Shear Driven (Wolfstein)
	Two-Layer ReY*: 60.0
	Two-Layer Delta ReY: 10.0
+-10 Reynolds-Averaged Navier-Stokes	
+-11 Segregated Volume Flux based Flow	Minimum Absolute Pressure: 1000.0 Pa
	Flow Boundary Diffusion: true
	Unsteady Flux Dissipation Corrections: false
	Limit Acoustic-CFL Option: Per-Model
	Secondary Gradients: On
	Convection: 2nd-order
	Delta-V Dissipation: Off
+-12 Three Dimensional	
+-13 Turbulent	
+-14 Two-Layer All y+ Wall Treatment	Iterative Ustar: false
+-15 VOF Waves	Damping Constant 1: 10.0
	Damping Constant 2: 10.0
	Damping Exponent: 2.0
	Enable Theory Comparison: false
	Forcing Constant: 10.0
`-1 Waves	
`-1 **FifthOrderVofWave 1**	Point On Water Level: [0.0, 0.205, 0.0] m
	Vertical Direction: [0.0, 1.0, 0.0]
	Advancing Direction: [1.0, 0.0, 0.0]
	Current: [0.0, 0.0, 0.0] m/s
	Wind: [0.0, 0.0, 0.0] m/s
	Additional Velocity: [0.0, 0.0, 0.0] m/s
	Wave Height: 0.03 m
	Water Depth: 0.6 m
	Specification Type: Wave Period
	First Wave Front Setting: true
	Light Fluid Density: 1.18415 kg/m^3
	Heavy Fluid Density: 997.561 kg/m^3
	Tags: []
`-1 Wave Period Specification	Wave Period: 1.0 s
	Wave Length: 1.5437730368270504 m
`-16 Volume of Fluid (VOF)	Convection: 2nd-order
	Compressibility Enhancement: false